Injectable, Cellular-Scale Optoelectronics with Applications for Wireless Optogenetics

Tae-il Kim *et al.*

Science **340**, 211 (2013);
DOI: 10.1126/science.1232437

Science (print ISSN 0036-8075; online ISSN 1095-9203) is published weekly, except the last week in December, by the American Association for the Advancement of Science, 1200 New York Avenue NW, Washington, DC 20005.

immune regulators, lymphoid disorganization, and virus persistence. IFN-I has pleiotropic effects on multiple cellular processes. Aside from antiviral effects (*25*), IFN-I signaling influences cell differentiation, proliferation, and apoptosis (*26*). Further, multiple pro-inflammatory mediators are downstream of IFN-I signaling; thus, IFN-I can regulate multiple physiological processes. Despite discovery of IFN-I over 50 years ago (*27*), its mechanisms of action with respect to immune modulation (*25*) or antiviral activity (*28*, *29*) remain unsettled.

Chronic immune activation after HIV infection is documented, and suppression of this hyperactivated state may alleviate pathologies associated with HIV infection (*7*). Disease after experimental simian immunodeficiency virus (SIV) infection in rhesus macaques correlates with elevated IFN-I and inflammatory signatures (*30*, *31*). In contrast, SIV infection in sooty mangabeys and African green monkeys, which develop modest pathology despite similar viral loads as macaques, correlates with reduced IFN-I and inflammatory signatures (*32*). Similar correlations with respect to reduced immune activation exist in HIV-infected elite controllers, although whether reduced immune activation follows better control of virus infection is debatable (*33*, *34*). Moreover, an elevated interferon signature is observed in HCV-infected patients despite limited control of virus replication and development of liver pathology (*35*, *36*). Thus, the IFN-I signaling pathway may be a viable target to control persistent viral infections.

References and Notes

1. D. G. Brooks *et al.*, *Nat. Med.* **12**, 1301 (2006).
2. D. L. Barber *et al.*, *Nature* **439**, 682 (2006).
3. J. S. Yi, M. A. Cox, A. J. Zajac, *Immunology* **129**, 474 (2010).
4. A. J. Zajac *et al.*, *J. Exp. Med.* **188**, 2205 (1998).
5. V. Appay, D. Sauce, *J. Pathol.* **214**, 231 (2008).
6. J. J. Chang, M. Altfeld, *J. Infect. Dis.* **202** (suppl. 2), S297 (2010).
7. G. d'Ettorre, M. Paiardini, G. Ceccarelli, G. Silvestri, V. Vullo, *AIDS Res. Hum. Retroviruses* **27**, 355 (2011).
8. N. Sevilla *et al.*, *J. Exp. Med.* **192**, 1249 (2000).
9. R. Ahmed, A. Salmi, L. D. Butler, J. M. Chiller, M. B. Oldstone, *J. Exp. Med.* **160**, 521 (1984).
10. M. Salvato, P. Borrow, E. Shimomaye, M. B. Oldstone, *J. Virol.* **65**, 1863 (1991).
11. C. F. Evans, P. Borrow, J. C. de la Torre, M. B. Oldstone, *J. Virol.* **68**, 7367 (1994).
12. B. M. Sullivan *et al.*, *Proc. Natl. Acad. Sci. U.S.A.* **108**, 2969 (2011).
13. A. Bergthaler *et al.*, *Proc. Natl. Acad. Sci. U.S.A.* **107**, 21641 (2010).
14. S. Scheu, P. Dresing, R. M. Locksley, *Proc. Natl. Acad. Sci. U.S.A.* **105**, 20416 (2008).
15. M. Macal *et al.*, *Cell Host Microbe* **11**, 617 (2012).
16. K. C. Sheehan *et al.*, *J. Interferon Cytokine Res.* **26**, 804 (2006).
17. N. Sevilla, D. B. McGavern, C. Teng, S. Kunz, M. B. Oldstone, *J. Clin. Invest.* **113**, 737 (2004).
18. M. B. Oldstone, K. P. Campbell, *Virology* **411**, 170 (2011).
19. S. Müller *et al.*, *J. Virol.* **76**, 2375 (2002).
20. D. P. Berger *et al.*, *Virology* **260**, 136 (1999).
21. M. Suresh *et al.*, *J. Virol.* **76**, 3943 (2002).
22. M. Zeng *et al.*, *J. Clin. Invest.* **121**, 998 (2011).
23. M. Zeng *et al.*, *PLoS Pathog.* **8**, e1002437 (2012).
24. B. Hahm, M. J. Trifilo, E. I. Zuniga, M. B. Oldstone, *Immunity* **22**, 247 (2005).
25. D. B. Stetson, R. Medzhitov, *Immunity* **25**, 373 (2006).
26. L. C. Platanias, *Nat. Rev. Immunol.* **5**, 375 (2005).
27. A. Isaacs, J. Lindenmann, *Proc. R. Soc. Lond. B Biol. Sci.* **147**, 258 (1957).
28. J. W. Schoggins, C. M. Rice, *Curr. Opin. Virol.* **1**, 519 (2011).
29. J. W. Schoggins *et al.*, *Nature* **472**, 481 (2011).
30. O. Manches, N. Bhardwaj, *J. Clin. Invest.* **119**, 3512 (2009).
31. B. Jacquelin *et al.*, *J. Clin. Invest.* **119**, 3544 (2009).
32. S. E. Bosinger *et al.*, *J. Clin. Invest.* **119**, 3556 (2009).
33. S. G. Deeks, B. D. Walker, *Immunity* **27**, 406 (2007).
34. A. Sáez-Cirión, G. Pancino, M. Sinet, A. Venet, O. Lambotte, *Trends Immunol.* **28**, 532 (2007).
35. A. I. Su *et al.*, *Proc. Natl. Acad. Sci. U.S.A.* **99**, 15669 (2002).
36. L. G. Guidotti, F. V. Chisari, *Annu. Rev. Pathol.* **1**, 23 (2006).

Acknowledgments: The authors thank D. Fremgen, C. Cubitt, N. Ngo, and S. Rice for technical excellence. Data reported in the manuscript are tabulated in the main paper and in the supplementary materials. This research was supported by NIH grant AI09484 (M.B.A.O.); National Cancer Institute grants NCI CA43059 (R.D.S.) and U54AI057160 to the Midwest Regional Center of Excellence for Biodefense and Emerging Infectious Diseases Research (MRCE) (R.D.S. and M.B.A.O.); grants AI077719 and AI047140 (J.C.d.l.T.), postdoctoral training grants AI007354; and American Heart fellowships 11POST7430106 (J.R.T.), HL007195 (C.N.), and NS041219 (B.M.S.).

Supplementary Materials

www.sciencemag.org/cgi/content/full/340/6129/207/DC1
Materials and Methods
Figs. S1 to S6
Reference (*37*)

15 January 2013; accepted 28 February 2013
10.1126/science.1235214

Injectable, Cellular-Scale Optoelectronics with Applications for Wireless Optogenetics

Tae-il Kim,[1,2]* Jordan G. McCall,[3,4,5,6]* Yei Hwan Jung,[1]† Xian Huang,[1] Edward R. Siuda,[3,4,5,6] Yuhang Li,[7] Jizhou Song,[8] Young Min Song,[1] Hsuan An Pao,[1] Rak-Hwan Kim,[1] Chaofeng Lu,[9] Sung Dan Lee,[10] Il-Sun Song,[11] Gunchul Shin,[1] Ream Al-Hasani,[3,4,5] Stanley Kim,[1] Meng Peun Tan,[10] Yonggang Huang,[7] Fiorenzo G. Omenetto,[12,13] John A. Rogers,[1,10,11,14]*‡ Michael R. Bruchas[3,4,5,6]*‡

Successful integration of advanced semiconductor devices with biological systems will accelerate basic scientific discoveries and their translation into clinical technologies. In neuroscience generally, and in optogenetics in particular, the ability to insert light sources, detectors, sensors, and other components into precise locations of the deep brain yields versatile and important capabilities. Here, we introduce an injectable class of cellular-scale optoelectronics that offers such features, with examples of unmatched operational modes in optogenetics, including completely wireless and programmed complex behavioral control over freely moving animals. The ability of these ultrathin, mechanically compliant, biocompatible devices to afford minimally invasive operation in the soft tissues of the mammalian brain foreshadow applications in other organ systems, with potential for broad utility in biomedical science and engineering.

Electronic systems that integrate with the body provide powerful diagnostic and therapeutic capabilities for basic research and clinical medicine. Recent research establishes materials and mechanical constructs for electronic circuits, light-emitting diodes (LEDs), sensors, and other components that can wrap the soft, external surfaces of the brain, skin, and heart, for diverse functions in analytical measurement, stimulation, and intervention (*1*–*10*). A significant constraint in operating these devices, however, follows from their surface-mounted configurations and inability to provide direct interaction into the volumetric depths of the tissues. Passive penetrating electrodes or optical fibers with interconnections to externally located electronic control and/or acquisition systems or light sources can be valuable in many contexts, particularly in neuroscience, engineering, and surgery (*7*, *10*–*14*). Direct biological integration is limited by challenges from tissue lesions during insertion, persistent irritation, and engineering difficulties in thermal management, encapsulation, scalable interconnection, power delivery, and external control. Many of these issues constrain attempts to insert conventional, bulk LEDs into brain tissue (*15*) and to use semiconductor nanowire devices as cellular probes or active, in vitro tissue scaffolds (*3*, *16*). In optogenetics, engineering limitations of conventional, tethered fiber optic devices restrict opportunities for in vivo use and widespread biological application. As a solution, we developed mechanically compliant, ultrathin multifunctional optoelectronic systems

[1]Department of Materials Science and Engineering, Frederick Seitz Materials Research Laboratory, University of Illinois at Urbana-Champaign, Urbana, IL 61801, USA. [2]School of Chemical Engineering, Sungkyunkwan University (SKKU), Suwon 440-746, Korea. [3]Department of Anesthesiology, Division of Basic Research, Washington University School of Medicine, St. Louis, MO 63110, USA. [4]Washington University Pain Center, Washington University School of Medicine, St. Louis, MO 63110, USA. [5]Department of Anatomy and Neurobiology, Washington University School of Medicine, St. Louis, MO 63110, USA. [6]Division of Biological and Biomedical Sciences, Washington University School of Medicine, St. Louis, MO 63110, USA. [7]Department of Civil and Environmental Engineering, Department of Mechanical Engineering, and Institute for Public Health and Medicine, Northwestern University, Evanston, IL 60208, USA [8]Department of Mechanical and Aerospace Engineering, University of Miami, Coral Gables, FL 33146, USA. [9]Soft Matter Research Center and Department of Civil Engineering, Zhejiang University, 38 Zheda Road, Hangzhou 310027, China. [10]Department of Electrical and Computer Engineering, University of Illinois at Urbana-Champaign, Urbana, IL 61802, USA. [11]Department of Mechanical Science and Engineering, University of Illinois at Urbana-Champaign, Urbana, IL 61802, USA. [12]Department of Biomedical Engineering, Tufts University, Medford, MA 02115, USA. [13]Department of Physics, Tufts University, Medford, MA 02115, USA. [14]Department of Chemistry, University of Illinois at Urbana-Champaign, Urbana, IL 61802, USA.

*These authors contributed equally to this work.
†Present address: Department of Electrical and Computer Engineering, University of Wisconsin-Madison, WI 53706, USA.
‡Corresponding author. E-mail: bruchasm@wustl.edu (M.R.B.); jrogers@uiuc.edu (J.A.R.)

that mount on releasable injection needles for insertion into the depths of soft tissue. These wireless devices incorporate cellular-scale components ranging from independently addressable multicolored microscale, inorganic light-emitting diodes (μ-ILEDs) to colocated, precision optical, thermal, and electrophysiological sensors and actuators.

A scanning electron micrograph (SEM) of an isolated gallium nitride (GaN) μ-ILED, a constituent component of these systems, is presented in Fig. 1A, as well as an epifluorescent image of a device among cultured human embryonic kidney (HEK293) cells, to illustrate the similar sizes. Each such "cellular-scale" μ-ILED (6.45 μm thick, 50 × 50 μm^2) uses high-quality epitaxial material grown on sapphire, processed to establish contacts (15 × 15 μm^2 square pads in the corners and an L-shaped current spreading layer for the p-type ohmic contact) and then released, to allow transfer printing onto narrow, thin plastic strips. The μ-ILEDs are less than one-thousandth the size of conventional LEDs (typically 100 μm thick, with lateral dimensions of 1 mm^2) and fiber optic probes, as discussed below (*17*). The small sizes of μ-ILEDs allow for spatially precise, cellular-scale delivery of photons, highly effective thermal management, reduced tissue damage, and minimized inflammation for prolonged use in vivo.

Combining μ-ILEDs with electronic sensors and actuators yields multifunctional integrated systems that can be configured in single or multilayer formats. The latter option is illustrated in Fig. 1, B and C, in which the sensors and/or actuators include a Pt microelectrode for electrophysiological recording or electrical stimulation (layer no. 1: a 20 × 20 μm^2 exposure defines the active area), a microscale inorganic photodetector (μ-IPD) based on an ultrathin silicon photodiode (layer no. 2: 1.25 μm thick, 200 × 200 μm^2), a collection of four μ-ILEDs connected in parallel (layer no. 3), and a precision temperature microsensor or microheater (layer no. 4: Pt serpentine resistor) (more details in figs. S1 to S3) (*18*). Each layer is processed on separate substrates shaped to match a releasable, photolithographically defined epoxy microneedle (fig. S4). A thin layer (~500 nm) of epoxy joins each of the layers in a precisely aligned, stacked configuration. The microneedle bonds to the bottom layer with a thin, bio-resorbable adhesive based on a film of purified silk fibroin, which enables removal of the microneedle after implantation (Fig. 1D, movie S1, and fig. S5). The microelectrodes measure extracellular voltage signals in the direct vicinity

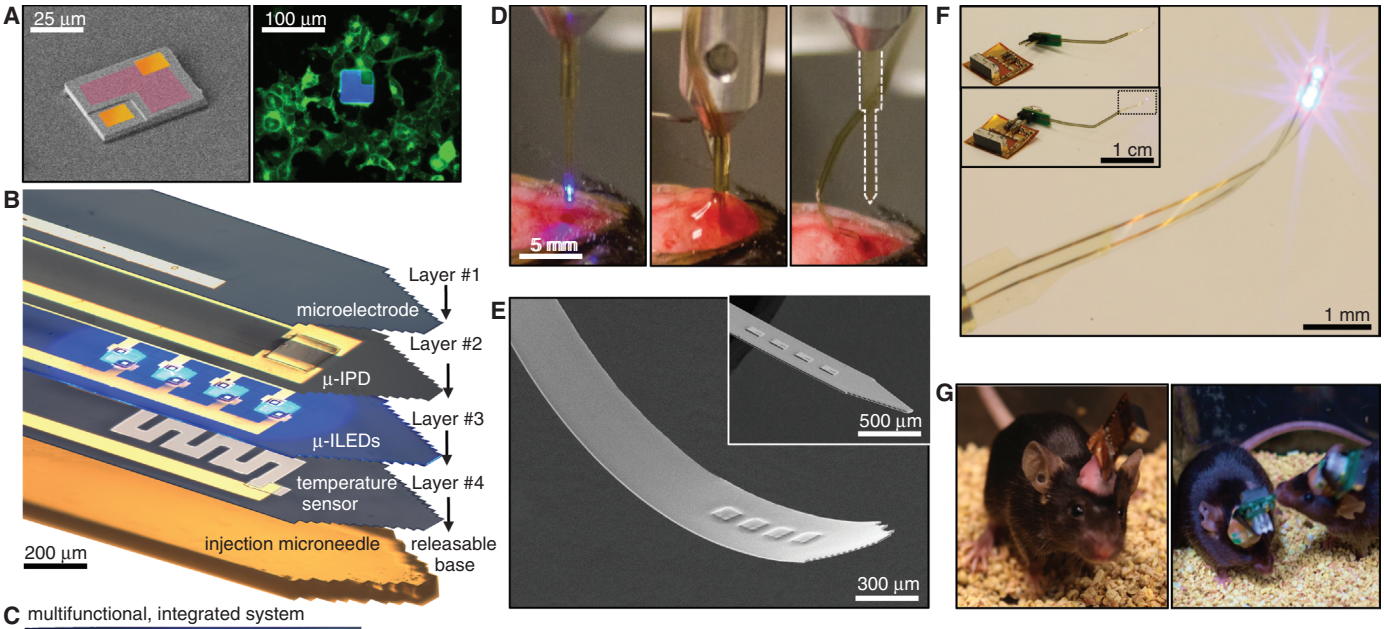

Fig. 1. Injectable, cellular-scale semiconductor devices, with multifunctional operation in stimulation, sensing, and actuation. (**A**) (Left) Colorized SEM (left) of a GaN μ-ILED (~6.45 μm thick, and 50 × 50 μm^2; contacts, gold; spreading layer, red). (Right) Fluorescent image of a μ-ILED (blue) with cultured HEK293 cells that express an eYFP-tagged transmembrane protein (green). (**B**) A multifunctional, implantable optoelectronic device, in a tilted exploded view layout illustrating various components. The system includes layers for electrophysiological measurement (no. 1: Pt contact pad, microelectrode), optical measurement (no. 2: silicon μ-IPD), optical stimulation (no. 3: μ-ILED array), and temperature sensing (no. 4: serpentine Pt resistor), all bonded to a releasable structural support for injection (microneedle). (**C**) Top view of the integrated device shown in (B). (**D**) Process of injection and release of the microneedle. After insertion, artificial cerebrospinal fluid (center) dissolves the external silk-based adhesive. The microneedle is removed (right), leaving only the active device components in the brain. (**E**) SEM of an injectable array of μ-ILEDs. The total thickness is 8.5 μm. (Inset) Rigid device before coating with a passivation layer. (**F**) Integrated system wirelessly powered with RF scavenging. (Insets) A connectorized device unplugged (top) and plugged into (bottom) the wireless power system. (**G**) Healthy, freely moving mice with lightweight, flexible (left) and rigid (right) wireless systems powering GaN μ-LED arrays in the VTA.

of illumination and can also be used for stimulation (Fig. 2H). The temperature sensors determine the degree of local heating, with a precision approaching ~1 mK, and can also be used as microheaters. The μ-IPD can measure the intensity of light from the μ-ILEDs while implanted deep in brain tissue and/or can enable basic spectroscopic evaluations such as absorption, fluorescence, and diffuse scattering (for details, see figs. S6 and S7) (*18*).

Injection of such flexible devices into the brain follows steps shown in Fig. 1D and movie S1. The injected multifunctional optoelectronic systems have a total thickness of ~20 μm. This exceptionally thin geometry, low bending rigidity, and high degree of mechanical flexibility (Fig. 1, E and F) allow for minimally invasive operation. Wired control schemes use standard transistor-transistor logic (TTL) and are therefore compatible with any readily available electrical commutator. Details on wired powering strategies and demonstration of wired optogenetic functionality in rodent behavioral assays are presented in figs. S8, S9, and S10 (*18*). Implementation of a wireless power module based on radiofrequency (RF) scavenging is shown in Fig. 1F. A custom flexible polyimide film–based lightweight (~0.7 g) power scavenger or a rigid printed circuit board–based scavenger (~2.0 g) (Fig. 1G and fig. S11) can be temporarily mounted on freely moving animals for short-term experimentation without constraint in natural animal behavior (Fig. 1G). The entire system consists of a wireless power transmitter and RF signal generator; an RF source (910 MHz, power output between 0.02 and 0.1 mW); a power supply; an RF power amplifier (gain of 49 dB at 910 MHz, power output between 1.6 and 7.9 W); and a panel antenna (gain of 13 dBi), as in fig. S11 and fig. S12. The low-frequency signal generator provides user-controlled amplitude modulation for programmed operation. The RF power that reaches the animals, under normal operating conditions at a distance of ~1 m, is between 0.15 and 0.77 mW/cm^2, which is substantially smaller than the maximum permissible exposure limits (3.03 mW/cm^2) for humans in controlled environments (*19*). Wireless control allows access to complex and ethologically relevant models in diverse environmental settings, including social interactions, home cage behaviors, wheel running, complex maze navigation tasks, and other behavioral outputs (Fig. 1G and fig. S13).

The electrical, optical, and thermal characteristics of the devices when operated in biological environments are important for optogenetics and other biomedical applications. The total optical power density of the four μ-ILEDs in this device as a function of electrical input power is shown in Fig. 2A (more details in figs. S14 and S15) (*18*). This performance is comparable to similarly designed, state-of-the-art conventional GaN LEDs (*17*). Many optogenetic constructs can be activated with ~1 mW/mm^2, at wavelengths near 450 nm (*13*). These conditions are well matched

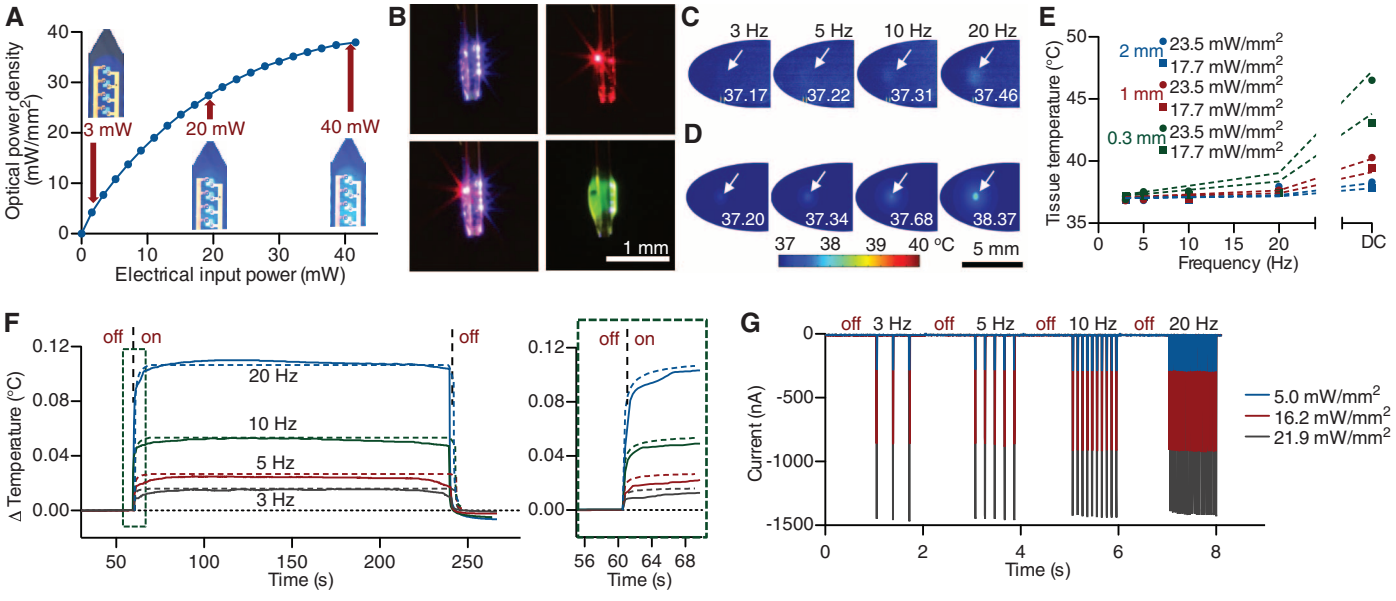

Fig. 2. Optical, thermal, and electrophysiological studies with corresponding theoretical analyses. (**A**) Total optical power density as a function of electrical input power applied to an array of four GaN μ-ILEDs; optical images show operation at 3, 20, and 40 mW. (**B**) A single device has one 675-nm GaAs μ-ILED and four 450-nm GaN μ-ILEDs that can be activated independently (top left and top right) or concurrently (bottom left). The same device is coated in a fluorescein sodium salt phosphor for 530-nm light (bottom right). (**C**) Measured and (**D**) calculated temperatures in explanted brain tissue near implanted μ-ILEDs at a depth of 0.3 mm and operated at 17.7 mW/mm^2 of light output power. (**E**) Temperatures in a system similar to that of (C) and (D), as a function of duty cycle in the operation of the μ-ILEDs and at three different implantation depths (0.3, 1.0, and 2.0 mm) and two different light output powers (17.7 and 23.5 mW/mm^2). (**F**) Change in brain temperature as a function of time, measured using an integrated temperature sensor colocated with an array of four μ-ILEDs in a lightly anesthetized mouse. Results evaluated at a peak input electrical power of 8.65 mW, in 3-, 5-, 10-, and 20-Hz pulses (10-ms duration). The vertical dashed lines indicate onset (at 60 s) and offset (at 240 s) of the μ-ILEDs. Colored dashed lines correspond to theoretical models for the temperature. The right frame shows the time dynamics as the device is powered. (**G**) Change in photocurrent as a function of time, measured using an integrated μ-IPD, for three different light output powers to an array of μ-ILEDs: 5.0 mW/mm^2 (blue trace), 16.2 mW/mm^2 (red trace), and 21.9 mW/mm^2 (black trace) at different pulse frequencies (10-ms pulses at 3, 5, 10, and 20 Hz). (**H**) Extracellular voltage trace (5 s) of spontaneous neuronal activity gathered using the integrated Pt microelectrode. (**I**) The same data are filtered and sorted using principal components analysis to identify single units.

to the output of the GaN μ-ILEDs. Input power of ~1.0 to 1.5 mW (Fig. 2A) is sufficient for both activation of the channelrhodopsin-2 [ChR2 (H134)] ion channel and precise control of intracellular signaling [adenosine 3′,5′-monophosphate (cAMP) and extracellular signal–regulated kinase (ERK 1/2)] via an optically sensitive seven-transmembrane domain receptor (OPTO-β2) (*20*) (Fig. 3, C and D, and figs. S16 and S17). Wirelessly, at a distance of 1 m, the RF scavenger produces 4.08 mW of electrical power resulting in a 7 mW/mm^2 optical power density. Other wavelengths are possible using different types of μ-ILEDs, either in multicolored or uniform arrays. An example of the latter, with blue and red (GaAs) μ-ILEDs, and the former, with green devices (produced using fluorescein sodium salt phosphor on a blue GaN μ-ILED), are shown in Fig. 2B.

μ-ILED–induced changes in temperature determined by infrared imaging and by analytical calculation, respectively, are shown in Fig. 2, C and D. The μ-ILEDs were implanted 0.3 mm into an explanted piece of brain tissue held at 37°C. The time-averaged temperatures measured at light-pulse (10-ms) frequencies of 3, 5, 10, and 20 Hz with peak light output of 17.7 mW/mm^2 are 37.17°, 37.22°, 37.31°, and 37.46°C, respectively. These results are similar to calculated time-averaged temperatures of 37.20°, 37.34°, 37.68°, and 38.37°C, respectively. Note that the input power used in these tests is 10 times what is necessary to activate many optogenetic constructs (*13*). The cellular-scale dimensions of the μ-ILEDs enable high rates of passive thermal spreading, and the brain tissue itself operates as an efficient heat sink. The latter is apparent in studies of the dependence of operating temperature on tissue thickness, operating power, and frequency (Fig. 2E). As in Fig. 2D, the experiment and theory agree remarkably well in spite of the indirect correlation between infrared imaging results and temperature at the location of the devices (details appear in figs. S18 and S19) (*18*). Perfusion in living tissue further increases the efficacy of these biological heat sinks. Changes in temperature measured in vivo using an integrated temperature sensor (fig. S6) compared with calculated results are shown in Fig. 2F. Collectively, these results indicate that changes in temperature associated with operation of μ-ILEDs can be less than 0.10°C for pulse frequencies less than 20 Hz, typical of many neuronal firing rates. These values are much lower than those that occur in human deep brain stimulation (DBS) regulation, ~2°C (*21*). Furthermore, in wireless operation, there is no appreciable change in temperature associated with operation at the head stage antenna or the skull (fig. S20).

Other components of this multifunctional platform exhibit similarly good characteristics. To demonstrate operation of the silicon μ-IPD, Fig. 2G shows photocurrents generated by different intensities of light from μ-ILEDs at different pulse frequencies. Finally, the Pt microelectrode has a 400 μm^2 exposure site with ~1.0 MΩ impedance at 1 kHz capable of measuring extracellular potentials on the microvolt scale necessary to distinguish individual action potentials (Fig. 2H), as demonstrated with clear clustering in the principal component analysis of spike data (Fig. 2I).

For use in optogenetics, such devices eliminate the need for lasers, bulk LEDs, fiber coupling systems, tethers, and optomechanical hardware used in conventional approaches (fig. S8). Furthermore, the fundamental optics of μ-ILEDs are very different from typical fiber optic implants. Absorbing and reflecting structures around the emissive areas of the μ-ILEDs enable precise delivery of light to cellular subregions. The

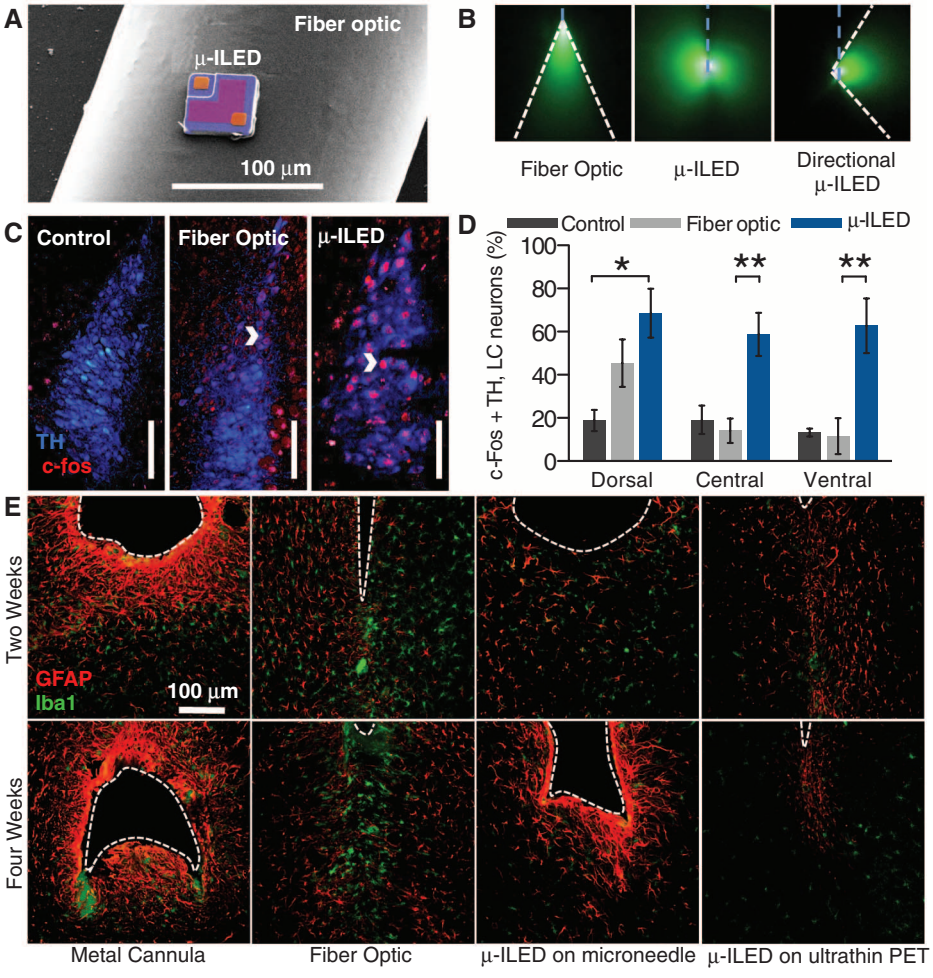

Fig. 3. μ-ILED devices improve spatial targeting and reduce gliosis. (**A**) Colorized SEM (left) of a μ-ILED mounted on a standard 200-μm fiber optic implant. (**B**) (Left) A dorsal-ventral–oriented light cone (outlined in white) from a 200-μm bare fiber implant (blue dash) emitting 465-nm light in 30 μM fluorescein water. (Center) Nearly omnidirectional light escape from a μ-ILED device (blue dash) with four 450-nm μ-ILEDs. (Right) Lateral light escape (outlined in white) from a modified μ-ILED device (blue dash) to allow unique spatial targeting, including flanking positions along the dorsal-ventral axis of brain loci. (**C**) Confocal fluorescence images of 30-μm brainstem slices containing the LC show staining for tyrosine hydroxylase (TH) and c-fos in control (left), fiber optic–implanted (center), and μ-ILED device–implanted (right) animals after 1 hour of 3-Hz photostimulation (15-ms pulses, 5-mW output power). Scale bar, 100 μm. (**D**) Fiber optic and μ-ILED treatments specifically increase coimmunoreactivity. In ventral portions of the LC, the μ-ILED devices express a higher proportion of TH (blue) and c-fos (red) coimmunoreactive neurons than fiber optic or control groups [n = 3 slices per brain from three brains for each group; two-way analysis of variance (ANOVA) with Bonferroni post hoc adjustment; all error bars represent means ± SEM; $^*P < 0.05$, $^{**}P < 0.01$]. (**E**) Confocal fluorescence images of 30-μm striatal slices show staining for astrocytes [glial fibrillary acidic protein (GFAP), red] and activated microglia (Iba1, green) at the ventral tip of each implanted device (dashed outline). Gliosis is smallest with the μ-ILED device at 2 and 4 weeks.

relative size and the different patterns of light emission from μ-ILEDs to fiber optic probes are shown in Fig. 3, A and B. Fiber optics typically approach brain structures dorsally. This approach preferentially illuminates cells in the dorsal portion of the targeted region with greater light intensity near the point of light escape (*22*) (Fig. 3B, left, and fig. S21). Targeting ventral cell bodies or terminals requires lesion of dorsal regions or the use of substantially greater, and potentially phototoxic (*23*), amounts of light to the site of interest. Neither option protects the intact architecture of a complete brain locus. Although recent advances have spatially restricted light from implanted fiber optics (*24*, *25*), these approaches require the use of invasive metal cannulae (Fig. 3E) or rely on sophisticated and sensitive optomechanical engineering that may limit their use in awake, behaving animals. The architecture of the μ-ILEDs enables light delivery medial or lateral to the intended target brain region. Native light escape from μ-ILEDs is nearly omnidirectional (Fig. 3B, center) but can be restricted to a wide range of angles with absorbing or reflective structures on the device (Fig. 3B, right).

We implanted both μ-ILEDs and fiber optics into animals expressing ChR2(H134)-eYFP (tagged with enhanced yellow fluorescent protein) in the locus coeruleus (LC) (fig. S21). One hour of output-matched photostimulation induced c-fos expression (*26*), a biochemical marker of neuronal activation, in both groups of ChR2(H134)-eYFP–expressing mice that was not seen in green fluorescent protein (GFP)–expressing controls (Fig. 3, C and D). The spatial distribution of c-fos expression, however, differed markedly between the fiber optic and μ-ILED groups. μ-ILED devices produced significantly greater activation in the ventral LC (Fig. 3D).

The physical sizes and mechanical properties of the μ-ILED systems reduce lesioning, neuronal loss, gliosis, and immunoreactivity. Glial responses are biphasic with an early phase featuring widespread activation of astrocytes and microglia and a late, prolonged phase hallmarked by restriction of the gliosis to the area closest to the implanted substrate (*27*). The μ-ILED devices produced substantially less glial activation and caused smaller lesions than metal cannulae and fiber optics, at both early (2 weeks) and late (4 weeks) phases (Fig. 3E). Furthermore, the brain tolerates the thin, flexible devices better than rigid structures (Fig. 3E), consistent with reports on passive electrode devices (*28*). Finally, we examined the chronic functionality of the devices and demonstrated that they are well tolerated in freely moving animals with encapsulated sensors and μ-ILEDs, which maintain function over several months (fig. S22).

We next implemented a fully wireless system for dissecting complex neurobiology and behavior. Phasic neuronal firing of ventral tegmental area (VTA)–dopaminergic (VTA-DA) neurons encodes salient stimuli and is sufficient for behavioral conditioning (*29*–*32*). We selectively targeted ChR2(H134)-eYFP to VTA-DA neurons (Fig. 4A) and tested whether mice would engage in wireless, optical self-stimulation (20 5-ms pulses every nose poke) of their dopamine reward pathway. To increase the contextual salience of the stimulation and to demonstrate wireless function of the μ-ILED devices, the mice were free to explore a complex environment (fig. S23, A to C). In the absence of physical reward, the same stimulation of VTA-DA neurons that drives a traditional conditioned place preference (fig. S9) (*29*, *30*) is actively sought with a cued nose poke when paired within a discrete environmental context. ChR2(H134)-eYFP mice learned to self-stimulate their dopamine neurons (Fig. 4, B and C) and, furthermore, developed a robust place preference (Fig. 4, D and E) for the environmental context containing the active nose poke for VTA-DA stimulation. ChR2(H134)-eYFP animals showed strong correlation (r = 0.8620, P = 0.0272) between the number of active nose pokes and the magnitude of conditioned place preference that was absent in eYFP controls (Fig. 4F and fig. S23E).

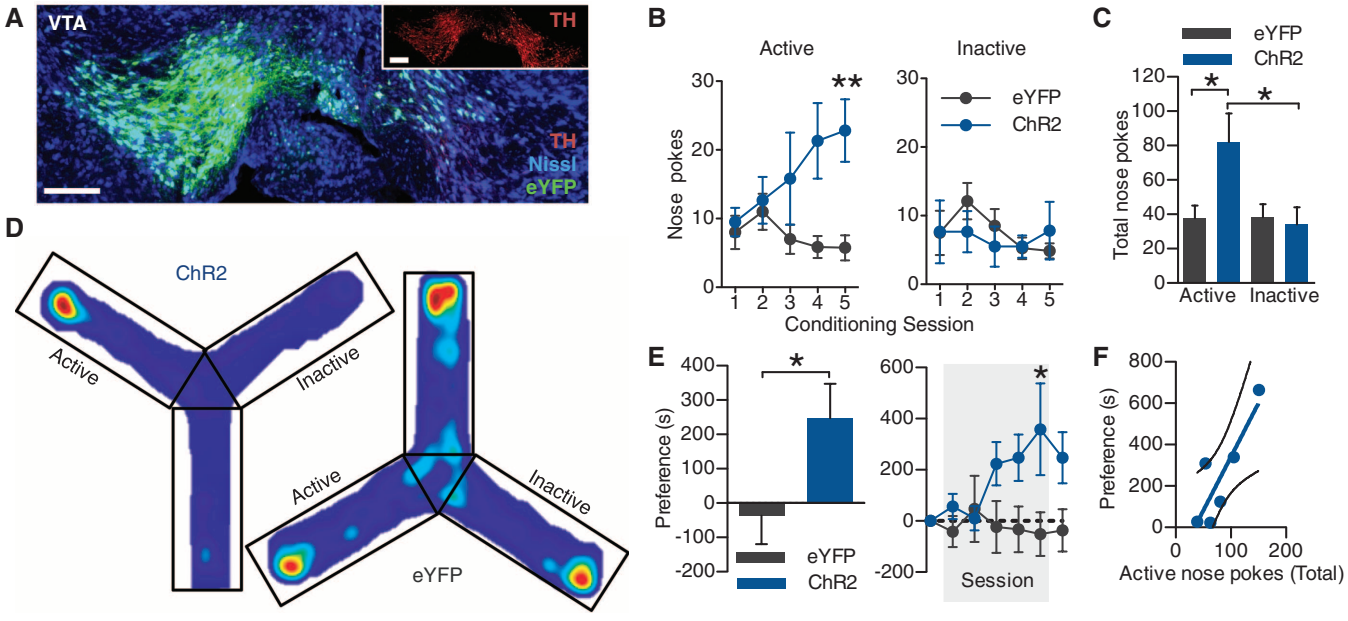

Fig. 4. Wirelessly powered μ-ILED devices operantly drive conditioned place preference. (**A**) Cell type–specific expression of ChR2(H134)-eYFP (green) in dopaminergic and TH-containing (red) neurons of the VTA. (Inset) For clarity, TH channel alone. All scale bars, 100 μm. (**B**) Operant learning curve on the active (left) and inactive (right) nose poke devices over 5 days of 1-hour trials in the Y maze. Each active nose poke drives 1 s of 20-Hz light (5-ms pulses) from the μ-ILED device (n = 6 to 8 mice/group; two-way ANOVA with Bonferroni post hoc adjustment; $^{**}P < 0.01$). (**C**) Mean number of nose pokes ± SEM across all five conditioning sessions ($^{*}P < 0.05$, one-way ANOVA with Bonferroni post hoc adjustment). (**D**) Heat maps of activity during the posttest; hotter colors represent longer duration in a location in that part of the apparatus. (**E**) (Left) Place preference scores calculated as posttest minus pretest in the active nose poke–paired context. Five days of self-stimulation significantly conditioned a place preference that developed over the course of the training sessions and remained during the posttest (right) ($^{*}P < 0.05$, t test compared with controls; $^{*}P < 0.05$, two-way ANOVA with Bonferroni post hoc adjustment). All error bars represent means ± SEM. (**F**) Scatter plot demonstrating positive correlation (r = 0.8620, P = 0.0272) between posttest preference and total number of active nose pokes during training in the ChR2(H134)-eYFP group.

In addition, we examined the effects of wireless tonic stimulation of VTA-DA neurons on anxiety-like behavior. Tonic stimulation at 5 Hz reduced anxiety-like behavior, whereas phasic activation of VTA-DA neurons did not have an effect on anxiety-like behavior (fig. S24). These findings are consistent with the anxiolytic actions of nicotine on VTA-DA neurons, as well as the behavioral phenotypes seen in the *Clock*Δ19 mice that have increased tonic firing of VTA-DA neurons (*33*, *34*), and further establish the utility of wireless optogenetic control in multiple environmental contexts.

These experiments demonstrate that these devices can be readily implemented in optogenetic experiments. Future possible uses are in closed-loop operation, where actuators (e.g., heat, light, and electrical) operate in tandem with sensors (e.g., temperature, light, and potential) for altering light stimulation in response to physiological parameters, such as single-unit activity, pH, blood oxygen or glucose levels, or neurochemical changes associated with neurotransmitter release. Many of the device attributes that make them useful in optogenetics suggest strong potential for broader utility in biology and medicine. The demonstrated compatibility of silicon technology in these injectable, cellular-scale platforms foreshadows sophisticated capabilities in electronic processing and biological interfaces. Biocompatible deep-tissue injection of semiconductor devices and integrated systems, such as those reported here, will accelerate progress in both basic science and translational technologies.

References and Notes

1. D.-H. Kim *et al.*, *Nat. Mater.* **9**, 511 (2010).
2. J. Viventi *et al.*, *Sci. Transl. Med.* **2**, 24ra22 (2010).
3. B. Tian *et al.*, *Science* **329**, 830 (2010).
4. D.-H. Kim *et al.*, *Science* **333**, 838 (2011).
5. Q. Qing *et al.*, *Proc. Natl. Acad. Sci. U.S.A.* **107**, 1882 (2010).
6. T. Sekitani, T. Someya, *MRS Bull.* **37**, 236 (2012).
7. J. Ordonez, M. Schuettler, C. Boehler, T. Boretius, T. Stieglitz, *MRS Bull.* **37**, 590 (2012).
8. S. C. B. Mannsfeld *et al.*, *Nat. Mater.* **9**, 859 (2010).
9. T. Sekitani *et al.*, *Science* **326**, 1516 (2009).
10. S. Takeuchi, T. Suzuki, K. Mabuchi, H. Fujita, *J. Micromech. Microeng.* **14**, 104 (2004).
11. E. Stark, T. Koos, G. Buzsáki, *J. Neurophysiol.* **108**, 349 (2012).
12. Y.-T. Kim, M. I. Romero-Ortega, *MRS Bull.* **37**, 573 (2012).
13. J. Mattis *et al.*, *Nat. Methods* **18**, 159 (2011).
14. P. Anikeeva *et al.*, *Nat. Neurosci.* **15**, 163 (2011).
15. H. Cao, L. Gu, S. K. Mohanty, J.-C. Chiao, *IEEE Trans. Biomed. Eng.* **60**, 225 (2013).
16. B. Tian *et al.*, *Nat. Mater.* **11**, 986 (2012).
17. T.-I. Kim *et al.*, *Small* **8**, 1643 (2012).
18. Materials and methods are available as supplementary materials on *Science* Online.
19. Federal Communications Commission (FCC), *Guidelines for Evaluating the Environmental Effects of Radiofrequency Radiation* (FCC publication docket no. 93-62, 1996); http://transition.fcc.gov/Bureaus/Engineering_Technology/Orders/1996/fcc96326.txt.
20. R. D. Airan, K. R. Thompson, L. E. Fenno, H. Bernstein, K. Deisseroth, *Nature* **458**, 1025 (2009).
21. M. M. Elwassif, Q. Kong, M. Vazquez, M. Bikson, *J. Neural Eng.* **3**, 306 (2006).
22. A. M. Aravanis *et al.*, *J. Neural Eng.* **4**, S143 (2007).
23. O. Yizhar, L. E. Fenno, T. J. Davidson, M. Mogri, K. Deisseroth, *Neuron* **71**, 9 (2011).
24. K. M. Tye *et al.*, *Nature* **471**, 358 (2011).
25. A. N. Zorzos, J. Scholvin, E. S. Boyden, C. G. Fonstad, *Opt. Lett.* **37**, 4841 (2012).
26. M. E. Carter *et al.*, *Nat. Neurosci.* **13**, 1526 (2010).
27. D. H. Szarowski *et al.*, *Brain Res.* **983**, 23 (2003).
28. T. D. Y. Kozai, D. R. Kipke, *J. Neurosci. Methods* **184**, 199 (2009).
29. H. C. Tsai *et al.*, *Science* **324**, 1080 (2009).
30. A. R. Adamantidis *et al.*, *J. Neurosci.* **31**, 10829 (2011).
31. I. B. Witten *et al.*, *Neuron* **72**, 721 (2011).
32. K. M. Kim *et al.*, *PLoS ONE* **7**, e33612 (2012).
33. T. M. McGranahan, N. E. Patzlaff, S. R. Grady, S. F. Heinemann, T. K. Booker, *J. Neurosci.* **31**, 10891 (2011).
34. L. Coque *et al.*, *Neuropsychopharmacology* **36**, 1478 (2011).

Acknowledgments: This work is supported by the NIH Common Fund; National Institute of Neurological Disorders and Stroke, NIH, R01NS081707 (M.R.B., J.A.R.); National Institute on Drug Abuse, NIH, R00DA025182 (M.R.B.); McDonnell Center for Systems Neuroscience (M.R.B.); National Security Science and Engineering Faculty Fellowship of Energy (J.A.R.); Division of Materials Sciences, U.S. Department of Energy, under award no. DE-FG02-07ER46471 (J.A.R.), and the Materials Research Laboratory and Center for Microanalysis of Materials (DE-FG02-07ER46453) (J.A.R.); and the Division of Biology and Biomedical Sciences, Washington University in St. Louis (WUSTL) (J.G.M.). We thank H. Tao (Tufts University) and S. Hwang (University of Illinois at Urbana-Champaign) for their help in preparation of silk solution and valuable discussions; the Bruchas laboratory and the laboratories of R. W. Gereau IV (WUSTL) and G. D. Stuber (University of North Carolina at Chapel Hill) for helpful discussions; K. Deisseroth (Stanford University) for the channelrhodopsin-2 (H134) and OPTO-β2 constructs; G. D. Stuber for the TH-IRES-Cre mice; the WUSTL Bakewell Neuroimaging Laboratory Core; and the WUSTL Hope Center Viral Vector Core.

Supplementary Materials

www.sciencemag.org/cgi/content/full/340/6129/211/DC1
Materials and Methods
Figs. S1 to S24
Table S1
References (*35*–*48*)
Movie S1

6 November 2012; accepted 18 February 2013
10.1126/science.1232437

Interactions Between the Nucleus Accumbens and Auditory Cortices Predict Music Reward Value

Valorie N. Salimpoor,[1,2,3]* Iris van den Bosch,[4] Natasa Kovacevic,[2] Anthony Randal McIntosh,[2] Alain Dagher,[1] Robert J. Zatorre[1,3]

We used functional magnetic resonance imaging to investigate neural processes when music gains reward value the first time it is heard. The degree of activity in the mesolimbic striatal regions, especially the nucleus accumbens, during music listening was the best predictor of the amount listeners were willing to spend on previously unheard music in an auction paradigm. Importantly, the auditory cortices, amygdala, and ventromedial prefrontal regions showed increased activity during listening conditions requiring valuation, but did not predict reward value, which was instead predicted by increasing functional connectivity of these regions with the nucleus accumbens as the reward value increased. Thus, aesthetic rewards arise from the interaction between mesolimbic reward circuitry and cortical networks involved in perceptual analysis and valuation.

Music is a potent phenomenon, existing in all cultures from prehistory onward (*1*). How sounds that have no intrinsic reward value can become highly pleasurable remains largely unknown. Prior studies demonstrate that listening to music engages not only the auditory cortices, but also emotion regions and reward-related mesolimbic circuits (*2*, *3*); studies have also shown that dopamine mediates this response in the striatum (*4*). These reward circuits reinforce biologically adaptive behaviors, including eating and sex (*5*, *6*), and are shared by most vertebrates. However, appreciation of music is complex and seemingly distinct to humans and is dependent on sociocultural factors, experience, and memory, suggesting an integrative role for cortical processes in interaction with dopamine-reinforcement circuits. Dopamine is involved in incentive salience and reward prediction, leading to expectation and anticipation

[1]Montreal Neurological Institute, McGill University, Montreal, Quebec H3A2B4, Canada. [2]The Rotman Research Institute, Toronto, Ontario M6A2E1, Canada. [3]BRAMS International Laboratory for Brain, Music and Sound Research, Montreal, Quebec, Canada. [4]Utrecht University, 3508 TC Utrecht, Netherlands.

*Corresponding author. E-mail: vsalimpoor@research.baycrest.org

www.sciencemag.org/cgi/content/full/340/6129/211/DC1

Supplementary Materials for

Injectable, Cellular-Scale Optoelectronics with Applications for Wireless Optogenetics

Tae-il Kim, Jordan G. McCall, Yei Hwan Jung, Xian Huang, Edward R. Siuda, Yuhang Li, Jizhou Song, Young Min Song, Hsuan An Pao, Rak-Hwan Kim, Chaofeng Lu, Sung Dan Lee, Il-Sun Song, Gunchul Shin, Ream Al-Hasani, Stanley Kim, Meng Peun Tan, Yonggang Huang, Fiorenzo G. Omenetto, John A. Rogers,* Michael R. Bruchas*

*Corresponding author. E-mail: bruchasm@wustl.edu (M.R.B.); jrogers@uiuc.edu (J.A.R.)

Published 12 April 2013, *Science* **340**, 211 (2013)
DOI: 10.1126/science.1232437

This PDF file includes

Other Supplementary Material for this manuscript includes the following:
(available at www.sciencemag.org/cgi/content/full/340/6129/211/DC1)

Materials and Methods

Preparation of μ-ILEDs

The fabrication began with epitaxially grown GaN on a sapphire wafer (500 μm thick double polished sapphire with 2" diameter, Cermet Inc.). The GaN stack layers consisted of undoped GaN (3.8 μm), n-type GaN (2 μm), spacer (0.4 μm), MQW (0.14 μm), and p-type GaN (0.2 μm). Residual metal ions and GaN oxide on the surface were removed by rinsing with diluted HCl (33 %). L-shaped current spreading layers of Ni (15 nm) and Au (15 nm) were formed by sputter deposition (AJA ATC 2000), followed by annealing at 500 ^{o}C for 5 min in an oxygen and nitrogen atmosphere to form an ohmic contact. After exposing n-type regions defined using photolithography (40 x 40 μm^2 recessive square with thick AZ 2035, Microchem Inc) and etched using chorine based-inductively coupled plasma reactive ion etching (ICP RIE, Plasmatherm, SLR-770), both n- and p- contact pads, each 25 x25 μm^2 in dimension, of 15 nm of Cr and 300 nm of Au were deposited by electron beam evaporation (Temescal, FC-1800). To define the lateral dimensions of the devices (100x100 μm^2), chorine based ICP RIE was used to remove GaN down to the sapphire substrate, with negative tone photoresist as an etching mask (AZ 2070, Micorchem Inc).

After deposition of a passivation layer of SiN_x (200 nm) by plasma enhanced chemical vapor deposition (PECVD; STS, Mesc Multiple) the processed substrate was bonded to a silicon wafer using a layer of palladium (Pd)-indium (In) chemical alloy, followed by laser lift off (KrF, intensity,~0.9 J/cm^2) to remove the sapphire from the μ-ILEDs. Here, the laser light triggered thermal decomposition at the GaN-sapphire interface, allowing easy mechanical removal of sapphire substrate upon heating to 70 ^{o}C on a hotplate. Wet etching with 5 wt% diluted HCl selectively removed the underlying unalloyed In layer, leaving residual porous structures of In-Pd alloy that served as anchors to tether the μ-ILEDs to the silicon wafer. In this configuration, the devices were easily lifted onto the surfaces of microstructured (3 μm in diameter, 1.2 μm in height, and 5 μm in space) slabs of poly(dimethylsiloxane) (PDMS; Sylgard 184, Dow Corning) via the action of van der Waals forces. Etching the exposed unalloyed Pd and passivation layer (SiN_x) removed all of residual metal on the μ-ILEDs. The result was an array of μ-ILEDs on microstructured PDMS, suitable for manipulation by transfer printing, for integration onto microneedles.

Fabrication of releasable, injection microneedles

To fabricate penetrating polymeric microneedles, suitable shapes were first defined in layers of Cr (15 nm) and Au (300 nm) deposited on a glass slide (5 x 3.5 cm^2) by photolithography and wet etching. Photo-curable epoxy (SU-8 100, Microchem Inc) was then spin cast (1100 rpm for 250 μm and 1800 rpm for 150 μm thickness) on the slide, and ultraviolet light was passed (380 mJ/cm^2) through the backside to define a pattern of exposure in the epoxy, with the geometry of the microneedle. Developing away the unexposed regions followed by thermal annealing (150 ^{o}C for 10 min) defined and fully cured the epoxy to complete the fabrication of microneedles, typically in array geometries. Poor adhesion between the glass and the epoxy allowed easy mechanical removal of the microneedles, with tweezers, stamps or other implements. The left image of Fig S5 shows an array of epoxy microneedles on glass. The left and right three microneedles were removed before this image was collected.

To fabricate 6 μm thick (or 2.5 μm thick for μ-ILED) polyester device substrates (Mylar® film, Chemplex® industries) with similar microneedle layouts, the films were first laminated on a

PDMS coated substrate. Patterns of Cr (100 nm thickness) in microneedle geometries were used as etching masks for oxygen plasma RIE (March polymer RIE) of the exposed regions of the films. Wet etching of the Cr completed the fabrication.

Fabrication of sensors

For microelectrodes and temperature sensors, 6 μm thick, patterned polyester films on PDMS coated glass, formed according to procedures described above, were used. To fabricate the electrophysiological sensor, 100 μm wide and 100 nm thick lines of Pt were formed on the needle by photolithography and lift-off using negative tone resist (AZ 2070, Microchem Inc). To measure electrophysiological signals from a single nerve, an epoxy passivation layer (SU-8 2, Microchem Inc.) defined 20 x 20 μm^2 openings to the underlying Pt, as the sensing locations. For temperature sensors, 20 nm thick and 20 μm wide Pt serpentine structures served as resistors, connected by Au electrodes at both ends.

For the photodetectors, the top silicon layer of an silicon on insulator (SOI) wafer (1.25 μm thick silicon on a 400 nm thick layer of silicon dioxide on a silicon substrate, Soitec) was p- and n-doped sequentially through masking layers of silicon dioxide (900-nm thick) deposited by plasma-enhanced chemical vapor deposition and patterned by photolithography and etching. For p-doping, the sample was exposed to a boron source for 30 min at 1000 ^oC in an N_2 environment. The n- doping used a phosphorous source under the same conditions for 10 min. A single cell had a size of 200 μm x 200 μm including p- and n- doped parts with 200 μm x 40 μm (active area: 200 μm x 120 μm), isolated by reactive ion etching through the silicon layer in a geometry patterned by photolithography. The buried oxide layer of the SOI wafer was partially etched to slightly undercut slicon layer. Next, photolithography defined photoresist structures at the four corners of each square cell to hold the silicon layers to the underlying silicon wafer during complete removal of the silicon dioxide layer with HF.

Measurements on μ-IPD

The current responses of μ-IPDs at different current injection levels (0 to 9 mA) into four blue μ-ILEDs, in an array, were measured at biases of -5V to 5V. For time-dependent light response measurements, AC current with four different frequencies (i.e., 3, 5, 10, and 20 hz) were applied to the μ-ILEDs using a pulse generator (Global Specialities®). The current resonse of the μ-IPDs at a bias of -3V were measured for 8 s with a sampling rate of 160 Hz.

Impedance measurements on microelectrode

Impedance was measured using a potentiostat (Gamry instruments, reference 600) with phoshate buffered saline (PBS, Sigma-Aldrich). The PBS solution was diluted in 1 liter deionized water for 0.01 M, pH 7.4 at 25 ^oC. To measure impedance, we appied frequency ranging from 11.0 KHz to 1 KHz.

Fabrication of μ-ILED arrays and interconnects on microneedles

A PDMS stamp with posts (100 × 100 μm and heights of 100 μm) was positioned above μ-ILEDs on a structured PDMS slab and then used to remove an μ-ILED, one at a time, for integration onto a thin UV curable adhesive coated on a 2.5 μm thick microneedle shaped substrate (patterned polyester film on PDMS coated glass, fabricated using steps similar to those

described above for the sensors). The printing was performed using a modified mask aligner (Karl Suss, MJB). To form interconnected arrays of μ-ILEDs, the SiN_x passivation layer was first removed by reactive ion etching (RIE; Plasmatherm 790). Coating with an adhesion promoter (Dow, AP3000) and then a layer of photosensitive benzocyclobutene (6 μm thick; BCB) prepared the devices for backside exposure to ultraviolet light, through the transparent substrate. This light exposed the BCB in all regions except those above the opaque n-, and p-contact pads. Developing away the unexposed BCB (Advanced Developer, DS2100) and blowing with a stream of N_2 removed the residual developer, to complete the patterning process for via holes. After fully curing the BCB in an Ar atomosphere in a glove box at 210 ^oC for 3 hr, remaining BCB residues on the contacts were removed by oxygen RIE. To form metallization lines to the contacts, 15 nm of Cr and 300 nm of Au were sputter deposited, and then wet etched through a photopatterned layer of photoresist. Finally, an epoxy layer (2 μm thick, SU-8 2 Microchem) was spin cast and cured to form insulating coatings on the electrodes.

Forming multi-functional μ-ILED systems on releasable injection microneedles

Separately fabricated thermal and electrophysiological sensors and printed μ-ILEDs, each on polyester thin film substrates, were stacked in an aligned configuration on a penetrating epoxy microneedle substrate using a modified mask aligner (Karl Suss, MJB). A thin layer of UV curable epoxy (SU-8 2) served as an adhesive for bonding the sensors and the μ-ILEDs. For bonding the entire stack to the penetrating microneedle, a thin layer of purified silk (7 wt%) was used, to allow release of after implantation. After curing or drying, the adhesives in all cases have thicknesses of a few hundred nanometers.

Characterization of optical and thermal properties

Optical measurements of the emission spectra and light output were obtained with a spectrometer (HR4000 and FOIS-1 fiber optics integrating sphere, Ocean Optics). Thermal measurements were performed using a MWIR-based InDb thermal imager (InfraScope, GFI) with a base temperature of 37^oC.

Wired powering

μ-ILED devices were connected to a function generator (AMPI, Master-9 or Tektronix, AFG3022B) and TTL modulation (low 0V, high 4V) was used to power the μ-ILEDs at the stated frequencies and pulse widths.

Wireless powering and RF powering scavenger

The wireless power transmitter includes a low-frequency signal generator, an RF signal generator, a power supply, a RF power amplifier, and a panel antenna. The low-frequency signal generator outputs an amplitude modulation signal to modulate the RF power generator. The RF power amplifier that is powered by the power supply enlarges the modulated RF signal from the RF signal generator. The RF power is then transmitted from the panel antenna on 75 μm thick polyimide layer or commercialized PCB board.. The RF signal generator has a power output from -10 to -17 dBm at 910 MHz, which corresponds to a power ranging from 0.1 mW to 0.02 mW. The power amplifier has a gain of 49 dB, thus the power output from the power amplifier is from 1.6 to 7.9 W. Under an antenna gain of 13 dBi and at a distance that is approximately 1 meter away from the antenna, the RF power that reaches the mice is approximately 4 mW, given

an exposure area of the mice of ~32 cm^2. Mice with chronically implanted μ-ILED devices were acutely connected to the headstage antenna immediately prior to any wireless photostimulation.

Numerical modeling of temperature in the μ-ILEDs

A three dimensional (3D) model was established to study the temperature distributions in the system in the pulsed mode and DC mode. Eight-node, hexahedral brick elements in the finite element software ABAQUS were used to discretize the geometry. The μ-ILEDs are modeled as heat sources. The bottom surface of device was set as a constant temperature, while the other surfaces are free heat convection boundary with the convection heat transfer coefficient 25 $W/(m^2 \cdot K)$. The initial temperature of the device was set as the environmental temperature T_∞. The dimensions and layout of the device can be found in the main text. The microelectrodes and the sensors were neglected in the finite element simulations due to their small thickness (~300 nm) compared to that of other layer (~6 μm). The thermal conductivity, density and thermal capacity are 317 $W/(m \cdot K)$, 19300 kg/m^3 and 130 $J/(kg \cdot K)$ (*35*) for Au, 0.2 $W/(m \cdot K)$, 1190 kg/m^3 and 1200 $J/(kg \cdot K)$ for epoxy (*36*), 0.15 $W/(m \cdot K)$, 1050 kg/m^3 and 1270 $J/(kg \cdot K)$ for polyester (*37, 38*), 230 $W/(m \cdot K)$, 2330 kg/m^3 and 700 $J/(kg \cdot K)$ for μ-ILEDs (*17, 39*), and 0.29 $W/(m \cdot K)$, 1050 kg/m^3 and 2180 $J/(kg \cdot K)$ for BCB (*40*).

Figure S16 (A) shows the time-average temperature of μ-ILEDs operated in pulsed modes (3, 10, and 20 Hz) and DC mode at 5, 10, 15 and 20 mW input power when the background temperature is T_∞ = 37 °C. The finite element results (line) agree well with the experimental measurements (dot). Figure S16 (B) and (C) show the surface temperature distribution from experiments and finite element simulations. They agree reasonably well with each other and the discrepancy is due to the assumption of heat source only for μ-ILEDs since other parts (e.g., Au interconnect) may also serve as heat sources.

Analytical modeling of temperature in the tissue

An analytical model was established to obtain the steady temperature in the tissue when the device is inserted into the mouse brain tissue. The μ-ILED is modeled as a disk heat source with a radius $r_0 = L/\sqrt{\pi}$ corresponding to the same area of μ-ILED ($L \times L$) and a heat generation of $Q(t)$. Since the thickness of tissue (~4 mm) is much larger than that of device (~100 μm), we ignore the device structure in the analytical modeling. Once we have the temperature due to a single μ-ILED, the temperature due to four μ-ILEDs can be obtained by the superposition theorem.

The heat transfer equation in cylindrical coordinate with the origin as the center of μ-ILED is

$$\frac{\partial^2 T}{\partial r^2} + \frac{1}{r}\frac{\partial T}{\partial r} + \frac{\partial^2 T}{\partial z^2} - \frac{c\rho}{k}\frac{\partial T}{\partial t} = 0 \quad (1)$$

where k is thermal conductivity of tissue, ρ is density of tissue, c is specific heat capacity of tissue. The thermal diffusivity of tissue is $\alpha = k/(c\rho)$. By setting $\theta = T - T_\infty$, where T_∞ is the remote temperature, the above equation becomes

$$\frac{\partial^2 \theta}{\partial r^2} + \frac{1}{r}\frac{\partial \theta}{\partial r} + \frac{\partial^2 \theta}{\partial z^2} = \alpha \frac{\partial \theta}{\partial t} \quad (2)$$

Boundary conditions involve the adiabatic condition on the top surface (z=-h_0) and a constant temperature T_∞ = 37 °C on the bottom surface (z=h_1). At the μ-ILED interface (z=0), discontinuous heat flow $Q(t)$ is assumed as a means to introduce the input pulsed power. Let's consider a unit pulsed power $P(t)$ for time between 0 an t_0 with a period T, which can be expanded into Fourier Series

$$P(t) = \begin{cases} 1 & 0 < t \le t_0 \\ 0 & t_0 < t \le T \end{cases} = a_0 + \sum_{n=1}^{\infty} a_n \cos n\omega t + \sum_{n=1}^{\infty} b_n \sin n\omega t \quad (3)$$

where $\omega = 2\pi / T, a_0 = t_0 / T, a_n = 2\sin(n\omega t_0)/(n\omega T), b_n = 2[1-\cos(n\omega t_0)]/(n\omega T)$. For each cos(*nwt*) [or sin(*nwt*)] in the power expression of Eq. (3), we can assume the solution of Eq. (2) to be $\theta(r,z,t) = \psi(r,z)\exp(n\omega t i)$. Equation (2) then becomes

$$\frac{\partial^2 \psi}{\partial r^2} + \frac{1}{r}\frac{\partial \psi}{\partial r} + \frac{\partial^2 \psi}{\partial z^2} - q^2 \psi = 0 \quad (4)$$

where $q^2 = \frac{n\omega i}{\alpha}$. Equation (4) can be solved by applying the Hankel transformation. For $-h_0 \le z \le 0$, we obtain the solution as

$$\psi(r,z;n\omega) = \int_0^{+\infty} A_0 \left[\exp(z\sqrt{s^2+q^2}) + \exp(-z\sqrt{s^2+q^2} - 2h_0\sqrt{s^2+q^2})\right] J_0(sr)\, s\, ds, \quad (5)$$

where $A_0 = \frac{r_0 J_1(sr_0)}{2k_s s\sqrt{s^2+q^2}} \frac{1-\exp(-2h_1\sqrt{s^2+q^2})}{1+\exp(-2h_0\sqrt{s^2+q^2} - 2h_1\sqrt{s^2+q^2})}$.

The temperature increase due to the power of cos(*nwt*) [or sin(*nwt*)] is then equal to $|\psi(r,z;n\omega)|\cos(n\omega t + \beta_n)$ [or $|\psi(r,z;n\omega)|\sin(n\omega t + \beta_n)$] where $\tan(\beta_n) = \mathrm{Im}(\psi)/\mathrm{Re}(\psi)$. The temperature due to the power *P(t)* in Eq. (3) is given by

$$\psi(r,z,t) = a_0\psi(r,z;0) + \sum_{n=1}^{\infty} a_n |\psi(r,z;n\omega)|\cos(n\omega t + \beta_n) + \sum_{n=1}^{\infty} b_n |\psi(r,z;n\omega)|\sin(n\omega t + \beta_n) \quad (6)$$

The temperature due to the four μ-ILEDs with total power $Q(t)$=Q_0*$P(t)$/4 can then be given by

$$\psi_{tot}(r,z,t) = \frac{Q_0}{4}\sum_{i=1}^{4} \psi_i(r,z,t) \quad (7)$$

In vitro experiments, the thermal conductivity k of the issue is 0.6 W/(m·K), the density ρ is 1040 Kg/m^3, the specific heat c is 3650 J/(kg·K)(*21*). The predicted surface temperature (z=-h_0) agrees well with experimental measurement as shown in Fig. S17, and Fig. 2(D) and (E). In vivo experiments, there is a heat loss due to blood flow and we fit an effective power to be 0.62 mW at 3Hz. Then the predicted the time-averaged temperature at the location of temperature sensor (z=-6 μm) agrees very well with that in experiments at other frequencies with ~5% error. To further verify the analytical solution in Eq. (7), a full 3D finite element model for the device/tissue system is also established. The time history of average temperature in Fig. 2(F) shows a good agreement between finite element simulation and experimental measurement.

Preparation of phantom skin and IR measurement of RF scavenger

The potential localized heating effect of RF power is characterized using a phantom skin sample that is placed in the RF field. The phantom skin (*41, 42*) is a gelatin-based material that is made of the combination of water, agar, polyethylene, sodium chloride, sodium azide (Sigma-Aldrich

Co.), and TX 151 (Oil Center Research), and has similar electrical properties as animal skin at the RF range. The thermal imaging is taken using an infrared camera (A655sc, FLIR Systems, Inc.), which has high resolution and a measurement accuracy at ±2% of the reading value.

Experimental subjects

Adult (25–35 g) male C57BL/6J and TH::IRES-Cre backcrossed to C57BL/6J mice were group-housed, given access to food pellets and water *ad libitum* (except where noted) and maintained on a 12 h:12 h light:dark cycle (lights on at 7:00 AM). All animals were held in a facility in the lab 1 week prior to surgery, post-surgery and throughout the duration of the behavioral assays to minimize stress from transportation and disruption from foot traffic. All procedures were approved by the Animal Care and Use Committee of Washington University and conformed to US National Institutes of Health guidelines.

Viral preparation

Plasmids coding pAAV-EF1a-DIO-EFYP, pAAV-EF1a-double floxed-hChR2(H134R)-EYFP-WPRE-HGHpA, and pLenti-EF1a-hChR2(H134R)-EYFP-WPRE were obtained from Addgene (Addgene.org) originally from the Deisseroth Laboratory at Stanford University. The DNA was amplified with a Maxiprep kit (Promega) and packaged into AAV5 serotyped viruses by the WUSTL Hope Center Viral Core. LV-PGK-GFP was provided by the WUSTL viral core facility. The final viral concentration was 2-5 x 10^{12} genome vg/mL for the adeno-associated viruses and 1.1-1.3 x 10^{8} IU/ml for all the lentivirus used.

Plasmid	**Source**	**Packaged by**	**Serotype**	**Titer**
pAAV-EF1a-DIO-EFYP	Deisseroth Laboratory (Stanford)	WUSTL Hope Center Viral Core	AAV5	5 x 10^12 vg/ml
pAAV-EF1a-double floxed-hChR2(H134R)-EYFP-WPRE-HGHpA	Deisseroth Laboratory (Stanford)	WUSTL Hope Center Viral Core	AAV5	2 x 10^13 vg/ml
pLenti-EF1a-hChR2(H134R)-EYFP-WPRE	Deisseroth Laboratory (Stanford)	WUSTL Hope Center Viral Core	N/A	1.1 x 10^{8} IU/ml
pRRLsinPGK-GFPppt	Sands Laboratory (WUSTL)	WUSTL Hope Center Viral Core	N/A	1.3 x 10^{8} IU/ml

Stereotaxic surgery

After the animals were acclimatized to the holding facility for seven to nine days, they were anaesthetized in an induction chamber (4% Isolflurane) and placed in a stereotaxic frame (Kopf Instruments, Model 1900) where they were maintained at 1-2% isoflurane. A craniotomy was performed and mice were injected with 1ul of AAV5-DIO-ChR2 or AAV5-DIO-eYFP, LV-Ef1α-ChR2-eYFP, or LV-Ef1α-GFP unilaterally into the VTA (stereotaxic coordinates from bregma: -3.20 anterior-posterior (AP), +/−0.50 medial-lateral (ML), −4.90 mm dorsal-ventral (DV)), LC (-5.45 AP, +/- 1.25 ML, -4.00 DV), or the ventral striatum (1.3 AP, +/- 1.0 ML, -4.00

DV). Mice were then implanted with metal cannula (PlasticsOne; coordinates adjusted from viral injection 0.00 AP, +/- 0.25 ML, +1.00 DV), fiber optic implants (coordinates adjusted from viral injection 0.00 AP, +/- 0.25 ML, +1.00 DV)(*43*), or a μ-ILED device (same coordinates as viral injection). Custom adapters (WUSTL Instrument Machine Shop) for the Kopf cannula holder (Model 1966) were used to implant the fiber optics and the μ-ILED devices. For biodissolvable samples, the device was implanted at the desired target, ACSF was applied to the portion of the device that remained outside of the skull to facilitate dissolution of the adhesive, and then the epoxy needle was removed after a delay of 15 minutes. The implants were secured using two bone screws (CMA, 743102) and affixed with TitanBond (Horizon Dental Products) and dental cement (Lang Dental). Mice were allowed to recover for 3-5 weeks prior to behavioral testing; this interval also permitted optimal AAV expression and Cre recombinase activity.

Immunohistochemistry

Immunohistochemistry was performed as described (*44*) Briefly, mice were anesthetized with pentobarbital and intracardially perfused with ice-cold 4% paraformaldehyde in phosphate buffer (PB). Brains were dissected, post-fixed for 24 hr at 4 ºC and cryoprotected with solution of 30% sucrose in 0.1M PB at 4ºC for at least 24 hr, cut into 30 μm sections and processed for immunostaining. 30 μm brain sections were washed three times in PBS and blocked in PBS containing 0.5% Triton X-100 and 5 % normal goat serum. Sections were then incubated for ~16 hr at room temperature in rabbit anti c-fos antibody (1:20000, Millipore), guinea pig anti-GFAP (1:500, Synaptic Systems), rabbit anti-Iba1 (1:300, Wako Chemicals) and/or chicken anti-TH (1:2000, Aves Labs). Following incubation, sections were washed three times in PBS and then incubated for 2 hr at room temperature in Alexa Fluor 488 goat anti-mouse IgG (1:500, Invitrogen), Alexa Fluor 594 goat anti-rabbit IgG (1:500, Invitrogen-), goat anti-chicken Alexa Fluor 633(1:500, Invitrogen) and/or goat anti-guinea pig Alexa Fluor 546(1:500, Invitrogen) were then washed three times in PBS and followed by three 10-min rinses in PB and mounted on glass slides with Vectashield (Vector Labs) and sealed with nail polish for microscopy. All sections were imaged on both epifluorescent (Olympus BX61) and confocal (Olympus Fluoview 500) microscopes. Gain and exposure time were constant throughout, and all image groups were processed in parallel using Adobe Photoshop CS5 (Adobe Systems).

Antibody	**Species**	**Dilution**	**Source**
GFAP	Guinea Pig	1:500	Synaptic Systems
Iba1	Rabbit	1:300	Wako Chemicals
TH	Chicken	1:2000	Aves Labs
c-fos	Rabbit	1:20,000	Millipore
Alexa Fluor 488 anti-mouse IgG	Goat	1:500	Invitrogen
Alexa Fluor 594 anti-rabbit IgG	Goat	1:500	Invitrogen
Alexa Fluor 633 anti-chicken IgG	Goat	1:500	Invitrogen
Alexa Fluor 546 anti-guinea pig IgG	Goat	1:500	Invitrogen
Alexa Fluor 594 anti-chicken IgG	Goat	1:500	Invitrogen

Cell culture and transfection of NOPR-YFP expressing, HEK293 Cells

A single 50 x 50 x 6.45 μm μ-ILED was printed onto a standard glass coverslip (Fisherbrand, 12-545-80). The glass was coated with Poly-L-lysine (Sigma-Aldrich, P4707) to facilitate cell adhesion. Stable HEK293 cells expressing pcDNA3 containing nociceptin opioid peptide receptor-YFP (NOPR-YFP) were generated as previously described (*45*). The NOPR-YFP expressing cells were grown on the coverslip in a 24-well plate and placed in a 37 °C 5% CO_2 incubator. Cells were washed three times with PBS and then fixed in 4% paraformaldehyde for 20 min, washed in PBS, washed in 0.1 M PB, and mounted using VECTASHIELD (Vector Laboratories) and sealed with clear nail polish. Images were captured using Metamorph 7.6 (Molecular Devices) and processed with ImageJ 1.44o (NIH).

cAMP Assay

HEK293 cells were co-transfected with Optoβ_2 (*20* and pGloSensor-22F cAMP plasmid (Promega E2301) in 96-well format. Using a SynergyMx microplate reader (BioTek; VT, USA), baseline luminescence recordings were taken. In the presence of 9-cis retinal (1μM), cells were exposed to μ-ILED light (450 nm, 5 sec, 0.5 W/cm^2 pulse) and relative luminescent units taken every 2 sec using GloSensor cAMP Assay (Promega). Relative luminescent units were normalized to an initial 1 min recording of baseline. Data are expressed as ± S.E.M.

Immunoblotting

Western blots for phospho-MAPKs were performed as described previously (*45*. Briefly, Optoβ_2 expressing HEK293 cells were serum-starved 4-6 h prior to treatment. Cells were light treated (450 nm, 1 min, 0.5 W/cm^2 pulse), lysed in 70 μl of lysis buffer (50 mM Tris-HCl, 300 mM NaCl, 1 mM EDTA, 1 mM Na3VO4, 1 mM NaF, 10% glycerol, 1% Nonidet P-40, 1:100 of phosphatase inhibitor mixture set 1 (Calbiochem), and 1:100 of protease inhibitor mixture set 1 (Calbiochem)), sonicated for 20 s, centrifuged for 15 min (14000 x g, 4 °C). 50 μg of total protein was loaded onto non-denaturing 10% bisacrylamide precast gels (Invitrogen) and run at 150 V for 1.5 h. Blots were transferred to nitrocellulose (Whatman, Middlesex, UK) for 1.5 h at 30 mV, blocked in TBS/5% bovine serum albumin for 1 hr, incubated overnight at 4 °C with a 1:1000 dilution of goat-anti- rabbit phospho-ERK 1/2 (Thr-202/Tyr-204) antibody (Cell Signaling) and mouse actin (1:20,000, AbCam). Following overnight incubation, membranes were washed 4 x 15 min in TBST (Tris- buffered saline, 1% Tween 20) and then incubated with IRDye 800- and 700 conjugated affinity-purified anti-rabbit or anti-mouse IgG at a dilution of 1:5000 (pERK) or 1:20,000 (actin) in a 1:1 mixture of 5% milk/TBS and Li-Cor blocking buffer (Li-Cor Biosciences, Lincoln, NE) for 1 h at room temperature, washed 3 x 10 min in TBST, 1 x 10 min in TBS and analyzed using the Odyssey infrared imaging system (Li-Cor Biosciences). Band intensity was measured using Odyssey software following background subtraction and integrated band density in high-resolution pixels calculated. All subtypes of ERK (1 and 2) were quantified together. All pERK bands were normalized to actin, as an equal protein loading control and plotted using GraphPad (GraphPad Prism 5.0) software. Statistical significance was taken as * $p < 0.05$ as determined by unpaired two-tailed t-test.

In vivo electrophysiology

To demonstrate the ability of the incorporated electrode, spontaneous cellular activity was monitored in the deep midbrain (Fig. 2H). For light modulated responses, an array of 16 (35-μm tungsten wires, 150-μm spacing between wires, 150-μm spacing between rows, Innovative Physiology) was epoxied to a rigid μ-ILED device and lowered into the VTA of a lightly (~1% isoflurane) anesthetized, TH-Cre mouse expressing ChR2(H134)-eYFP in the VTA (fig. S15). Two skull screws were arbitrarily placed anterior to bregma on either side of the midline and used to ground the electrode array. In either approach, voltage readings from each electrode were bandpass-filtered with activity between 250 and 8,000 Hz analyzed as spikes. The signal was amplified and digitally converted using commercially available hardware and software (Omniplex and PlexControl, Plexon). Spikes were sorted using principal component analysis and/or evaluation of t-distribution with expectation maximization (Offline sorter, Plexon).

Light path visualization

A 200 μm, 0.48 NA diameter fiber optic coupled to a 465 nm blue LED (Plexon) or devices with four, 100 x 100 x 6.45 μm 450 nm blue μ-ILEDs were adjusted to have the same (~280 μW) light output. The light sources were submerged in 30 μM fluorescein sodium salt (Sigma-Aldrich, F6377) (*24*) in deionized water and the photos were taken in a dark room with an exposure of 1/1000 s and an f-number of 5.6 from ~50 cm away for all images. Each photo was cropped using Photoshop (Adobe Systems), but no other processing was used.

c-fos expression

C57BL/6J mice were injected with LV-Ef1α-ChR2-eYFP or LV-PGK-GFP into the LC as described above. Three weeks later, animals were anesthetized, mounted on the stereotaxic instrument, and fiber optics or μ-ILED devices were acutely implanted to target the LC. 5 mW, 3 Hz blue light stimulation was delivered for 1 hour (*26*), animals were perfused immediately following, and immunohistochemistry was performed as above. Slices from the LC originated from approximately -5.45 mm caudal to bregma were mounted and imaged. For quantification, the LC was divided into three (dorsal, central, and ventral) 100 x 100 μm compartments. TH and c-fos labeled channels were separated, the compartment mask was applied, an exclusive threshold was set and positive staining for each channel was counted in a blind-to-treatment fashion using Metamorph. The counts from each channel were then overlaid and percent TH+ cells expressing c-fos were reported.

Immuno-glial response in implanted tissues

C57BL/6J mice (n=16) were implanted with devices into the ventral striatum and allowed to recover for either 2 or 4 weeks before perfusion. Immunohistochemistry was performed as described.

Conditioned Place Preference

VTA injected (AAV5-DIO-eYFP or AAV5-DIO-ChR2-eYFP; n=4-6/group) mice were trained in an unbiased, balanced three- compartment conditioning apparatus as described (*44*). Briefly, mice were pre-tested by placing individual animals in the small central compartment and allowing them to explore the entire apparatus for 30 min. Time spent in each compartment was recorded with a video camera (ZR90; Canon) and analyzed using Ethovision 8.5 (Noldus). Mice were randomly assigned to light and no-light compartments and received no light in the morning

and light (20, 5 ms pulses every minute) in the afternoon at least 4 h after the morning training on three consecutive days. CPP was assessed on day 5 by allowing the mice to roam freely in all three compartments and recording the time spent in each. Scores were calculated by subtracting the time spent in the light stimulus-paired compartment post-test minus the pre-test.

Real-time Place Preference

VTA injected (AAV5-DIO-eYFP or AAV5-DIO-ChR2-eYFP; n=3/group) TH-Cre mice were trained in an unbiased, balanced three-compartment conditioning apparatus as described (*44*) Mice were trained in the same conditioning apparatus as described above, and the pretesting phase (day 1) was identical. However, on days 2–4, mice were still allowed to freely roam all three compartments. On these conditioning days, entry into one compartment was paired with 20, 5 ms pulses of light that would repeat every minute the animal remained in the light-paired chamber. On day 5, the post-testing was identical as the above. Scores were calculated by subtracting the time spent in the light stimulus-paired compartment each day minus the pre-test.

Operantly Conditioned Place Preference

VTA injected (AAV5-DIO-eYFP or AAV5-DIO-ChR2-eYFP; n=6-8/group) TH-Cre mice were prepared for nose poke training by mildly restricting daily food to four grams to stabilize body weight and facilitate behavioral responding. Mice were trained in an unbiased, balanced three-compartment Y-Maze. Each arm of the Y-Maze was 50 cm by 10 cm, a 50 cm^2 equilateral triangle connected all three arms (for a total area of 1550 cm^2), and each arm was outfitted with a unique context (white, horizontal black stripes, or vertical black stripes). At the distal end of each of the striped arms a nose poke device (Med Associates, ENV-313M). On day 1, the headstage antenna was attached and mice were pre-tested by placing individual animals in the intersection of the three arms and allowing them to explore the entire apparatus for 30 min. During the pre-test and post-test sessions, a wall was placed to prohibit access to the nose poke apparatus and the final 15 cm of each arm. On days 2-6, the headstage antenna was attached and mice were allowed access to the entire Y-Maze for 1 hour. During these conditioning sessions a cue light was on to indicate a stimulation could be achieved nose poke and turned off for 500 ms following a poke on either device. A nose poke on the active device triggered an optical stimulation (20 pulses, 20 Hz, 5 ms pulse duration) on a fixed ratio-1 schedule, while a poke on the inactive device resulted in the cue light turning off for 500 ms. Nose pokes were recorded using a Med Associates TTL-I/O Interface connected to the Noldus Ethovision I/O Box. On day 7, the post-testing was conducted in an identical manner as the pre-test. All activity and position data was recorded using Ethovision and analyzed using Microsoft Excel and GraphPad Prism 5.0. Place preference scores were calculated by subtracting the time spent in the active nose poke-paired compartment each day minus the pre-test.

Open Field Test

OFT testing was performed in a sound attenuated room maintained at 23ºC. Lighting was measured and stabilized at 200 lux, and performed in the afternoon between 13:00–1600 hrs. The open field was a 55 x 55 cm square enclosure and was cleaned with 70% ethanol between testing trials. For testing, VTA injected (AAV5-DIO-eYFP or AAV5-DIO-ChR2-eYFP; n=6-8/group) TH-Cre mice were connected to cables coupled to a function generator and placed in the center of the open field and allowed to roam freely for 15 min. During the entire trial, animals received 20, 5 ms pulses of photostimulation. Movements were video- recorded and analyzed using

Ethovision. The center was defined as a square comprised of 50% the total area of the OFT. Time in the center expressed as percentages total time was the primary measure of anxiety-like behaviors.

Elevated Zero Maze

EZM testing was performed in a sound attenuated room maintained at 23ºC. Lighting was 200 lux, and performed in the afternoon between 13:00–1600 hrs. The EZM (Harvard Apparatus) was made of grey plastic (Dimensions: 200 cm in circumference comprised of four 50 cm sections: two opened, two closed. The maze was elevated 50 cm above the floor and had a path width of 4 cm with a 0.5 cm lip on each open section) and was cleaned with 70% ethanol between trials. For testing, VTA injected (AAV5-DIO-eYFP or AAV5-DIO-ChR2-eYFP; n=6-9/group) TH-Cre mice were connected to the headstage antenna and placed at the threshold of a closed section facing the open section and allowed to roam freely for 9 min. For the first and the final 3 minutes of each trial there was no photostimulation. For minutes 4-6, animals received 5 Hz, 5 ms width stimulation. Movements were video- recorded and analyzed using Ethovision (Noldus). Open section times expressed as percentages total time the primary measures of anxiety-like behaviors.

Data Analysis/Statistics

Data are expressed as means ± SEM. Data were normally distributed, and differences between groups were determined using independent t-tests or one-way ANOVA, or two-way ANOVAs followed by post hoc Bonferroni comparisons if the main effect was significant at $p < 0.05$. Statistical analyses were conducted using Prism 5.0 (GraphPad).

Genotyping of mouse lines

DNA was isolated from tail tissue obtained from weanling mice (21-28 days of age), and PCR screening was performed using the following primers: Cre recombinase (forward: 5'- GCA TTA CCG GTC GAT GCA ACG AGT GAT GAG-3' and reverse: 5'- GAG TGA ACG AAC CTG GTC GAA ATC AGT GCG-3') yielding a 400-bp PCR product in Cre positive animals. Fatty acid-binding protein intestinal primers (forward: 5'- TGG ACA GGA CTG GAC CTC TGC TTT CCT AGA-3' and reverse: 5'- TAG AGC TTT GCC ACA TCA CAG GTC ATT CAG-3') were used as positive controls and yield a 200-bp PCR product.

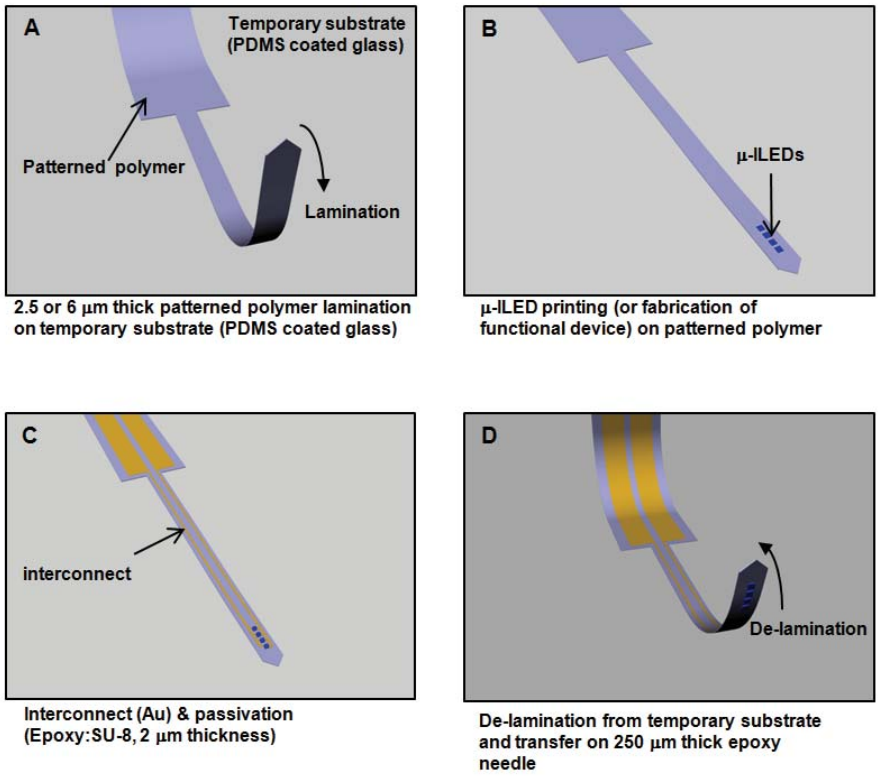

Figure S1

Schematic illustration of steps for fabrication **(A)** thin (2.5 or 6.0 μm thick) microneedle-shaped polymeric template laminated on a PDMS coated substrate, **(B)** μ-ILEDs integrated by transfer printing, **(C)** patterned passivation layers and interconnects, and **(D)** removal of the device from the PDMS coated substrate and transfer printing onto a releasable, injection microneedle substrate.

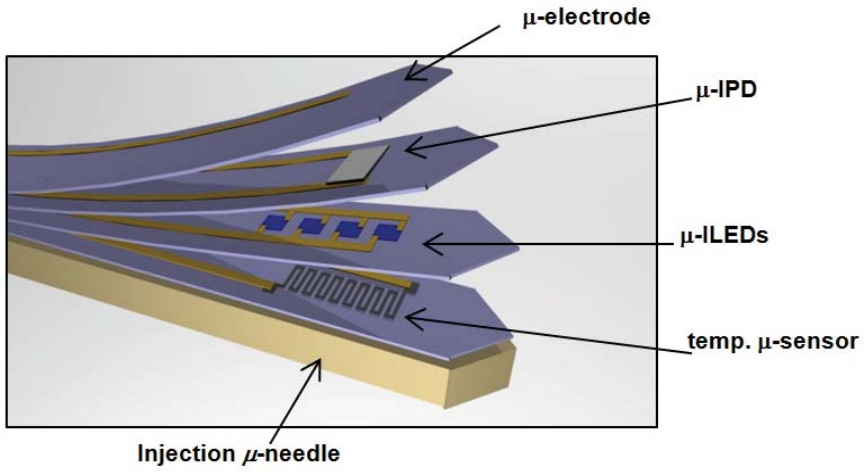

Figure S2

Schematic illustration of a printed multifunctional μ-ILED system.

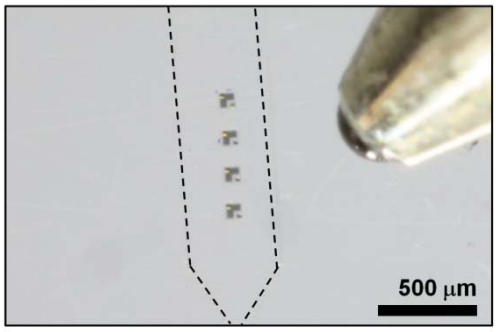

Figure S3

Photograph of four printed μ-ILEDs next to the tip of a ballpoint pen (right), to set the scale. Each μ-ILED has lateral dimensions of 100 x100 μm^2, with two 25x25 μm^2 metal pads for contacts and an L-shape current spreader.

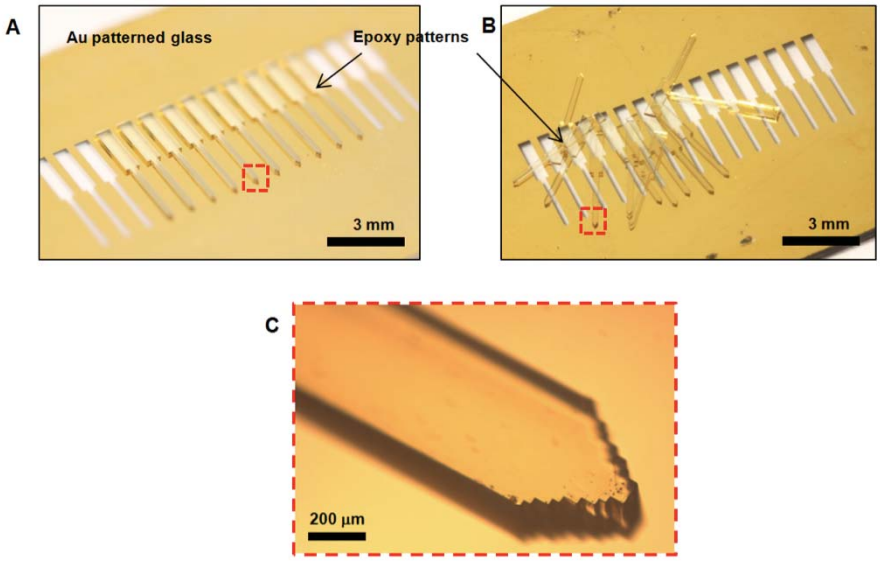

Figure S4

Images of injection microneedles defined photolithographically using a UV-curable epoxy (250 µm thick, SU-8 100). **(A)** Photolithographic patterning of epoxy on a pre-patterned glass substrate **(B)** microneedles delaminated by mechanical force from the glass substrate. **(C)** Tilted optical microscopic image of a single microneedle.

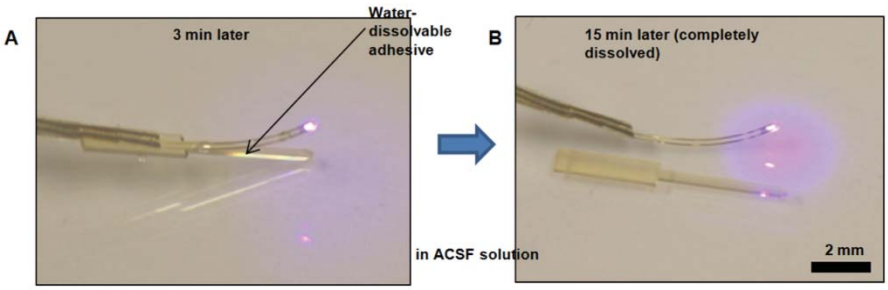

Figure S5

Demonstration of silk as a water soluble, bio-resorbable, releasable adhesive for injection microneedles. **(A)** Image of a device at the initial stages of silk dissolution, after 3 min and **(B)** after full dissolution and mechanical separation, after 15 min.

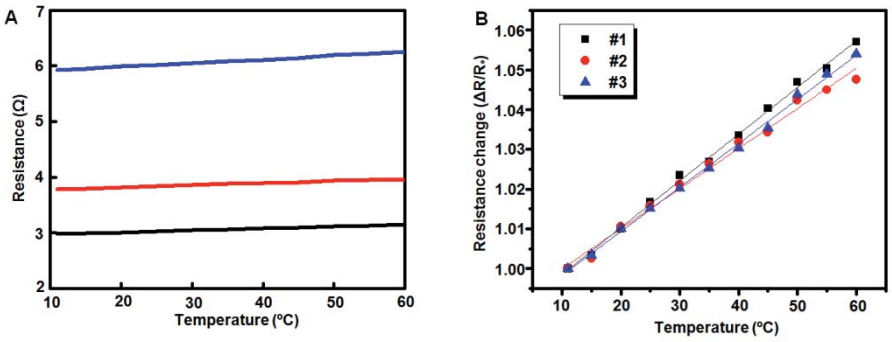

Figure S6

Relationship between temperature and resistance of temperature sensors. **(A)** Change in resistance with temperature. **(B)** Fractional change in resistance as a function of temperature, for three different devices.

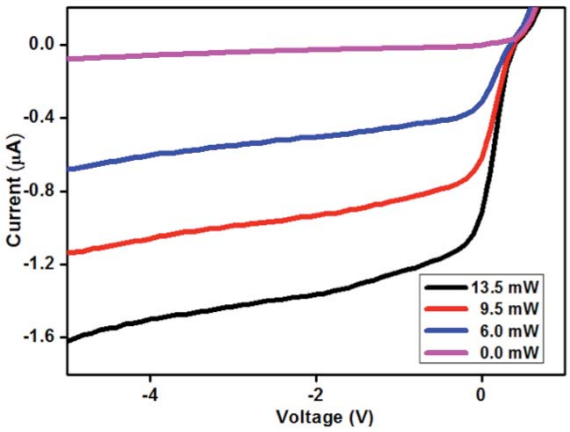

Figure S7

Current-voltage (I-V) characteristics of a μ-IPD exposed to different light intensities generated by operation of four μ-ILEDs. Electrical DC input powers into the μ-ILEDs were 0, 6.0, 9.5, 13.5 mW.

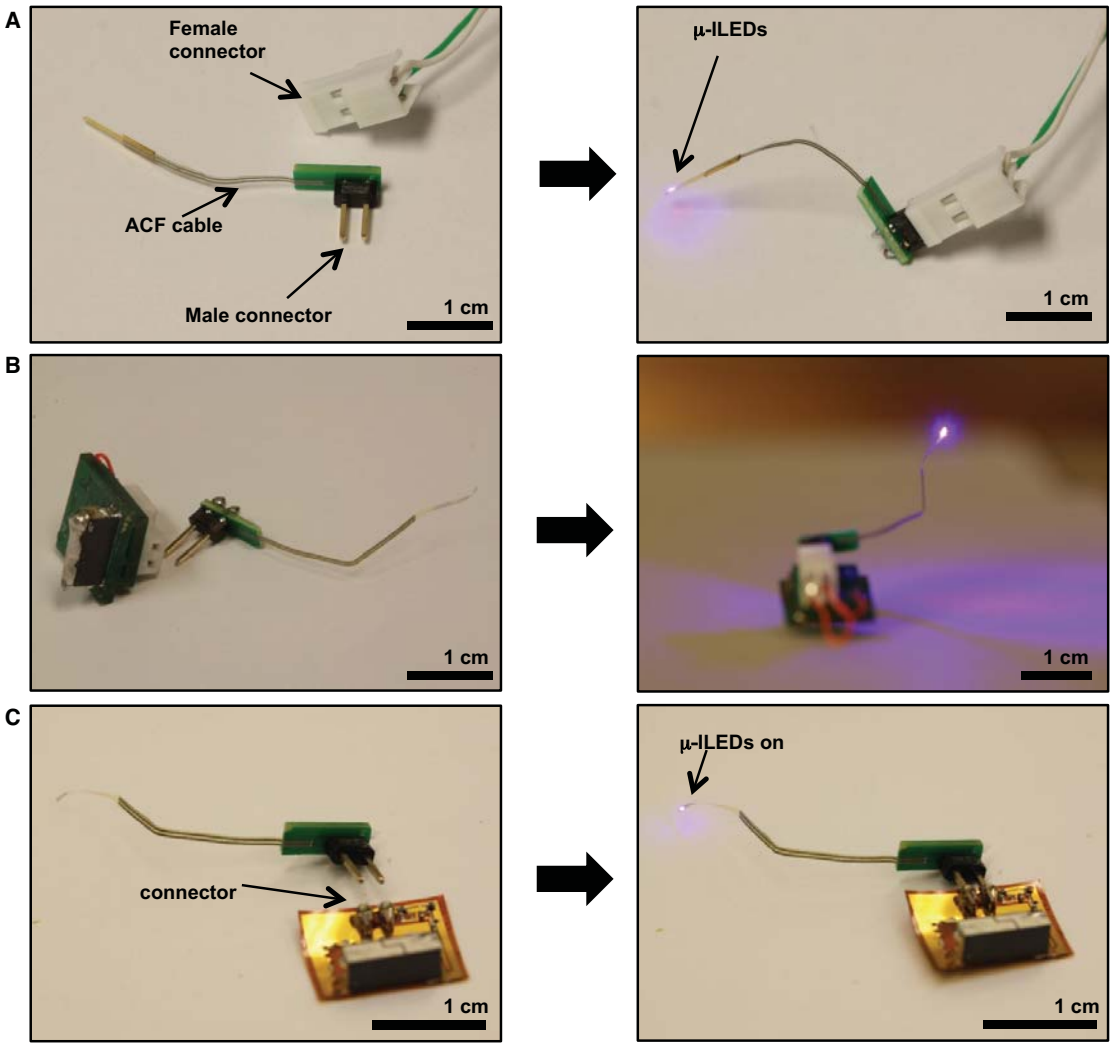

Figure S8

Images of the plug-in geometry of the connection between power supplies and penetrating μ-ILED systems, for the case of a wired supply **(A)** and RF wireless units **(B and C)**.

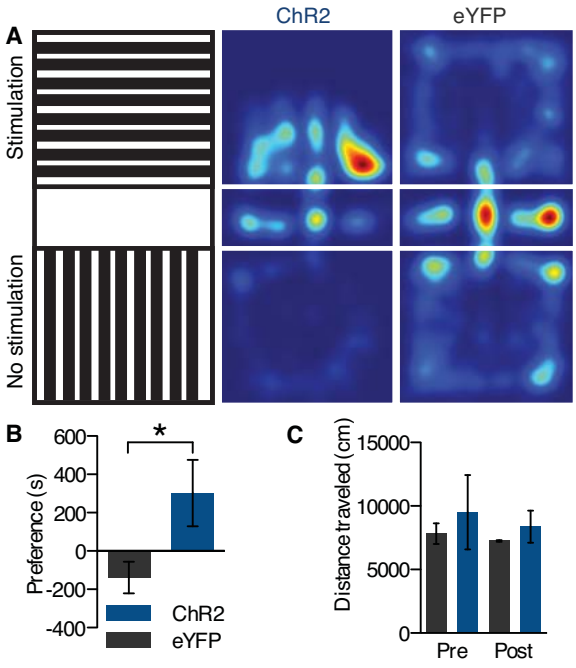

Figure S9

μ-ILED devices drive a conditioned place preference using standard TTL signals. To demonstrate wired functionality, we selectively targeted ChR2(H134)-eYFP to VTA-DA neurons (Fig. 4A) and tested that phasic activation (20, 5 ms pulses every minute) of cells with a μ-ILED device is sufficient to drive robust place preference behavior without a change in locomotor activity. Animals were conditioned over three days for 30 minutes. μ-ILED devices were powered and controlled using standard function generator (Tektronix, AFG3022B or AMPI, Master-9). (**A**) Left, Diagram of three-chambered conditioned place preference apparatus. Right, representative heat maps of activity during the post-test, hotter colors represent longer duration at every location in the apparatus. (**B**) Place preference scores, calculated as post-test minus pre-test on the light stimulation-paired side (n = 4-6/group; *$p<0.05$ t test compared to AAV5-DIO-eYFP controls). (**C**) Total activity during the pre- and post-tests shows no difference between the two groups. All bars represent means ± SEM.

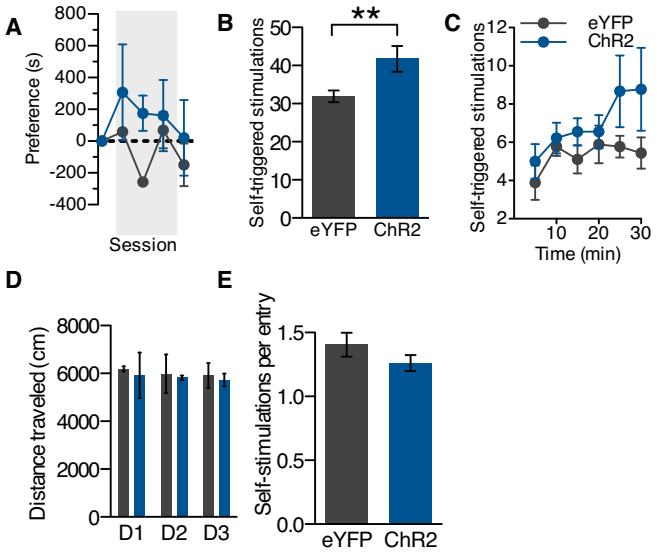

Figure S10

Real-time assessment of reward seeking or aversion is possible by pairing an animal's behavioral response with self-triggered stimulation or inhibition (*46-48*). Real-time conditioning, animals allowed free access to the apparatus from fig. S18A learn to self-trigger stimulations when 10, 5 ms pulses at 20 Hz light is delivered contingent on entry into the paired chamber. (**A**) Animals did not express either a real-time or conditioned place preference under this experimental design. (**B**) AAV5-DIO-ChR2 mice, however, did have increased numbers of passive, entry-triggered self-stimulations. (**C**) Passive self-stimulation is learned over the course of each trial. (**D**) Importantly, this difference is not due to a change in activity between the two groups (n = 3/group, **p<0.01 t test compared to AAV5-DIO-eYFP controls). (**E**) Animals could receive subsequent stimulations if they remained in the stimulus-paired chamber for 60 seconds. ChR2 mice did not learn to remain in the chamber for these subsequent stimulations.

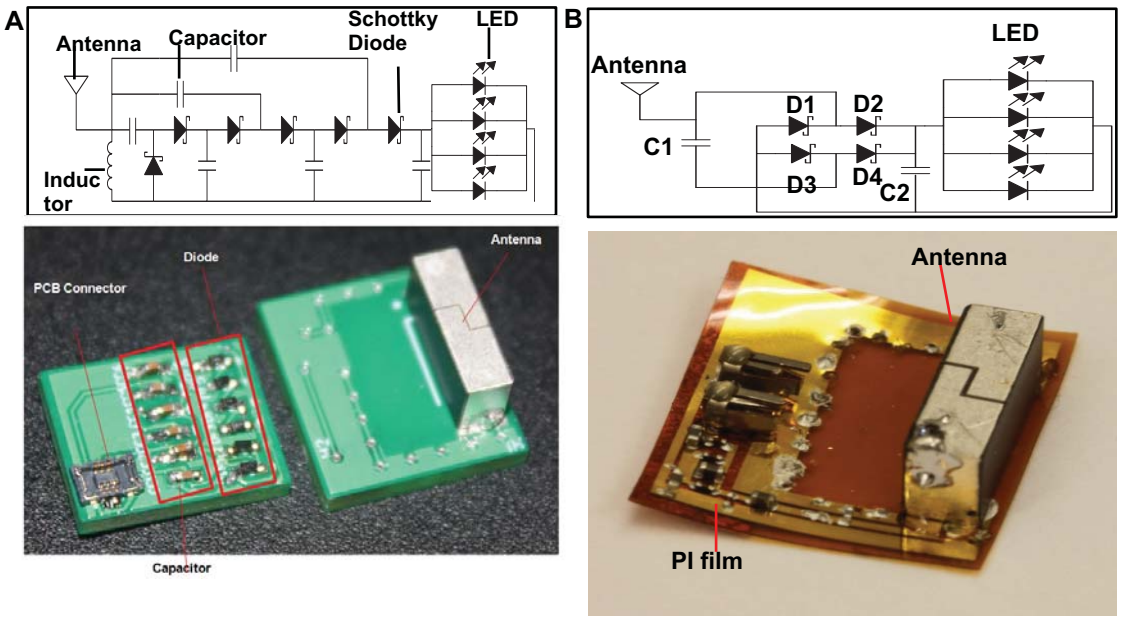

Figure S11

Circuit diagrams for each RF powering scavenger and pictures of RF powering scavenger (left) and RF antenna (right), in a miniaturized PCB layout (**A**) and on polyimide film (**B**). The RF power scavenger contains a RF antenna that works at 910 MHz, an impedance matching inductor, a voltage multiplexer with cascaded combination of Schottky diodes and capacitors, and blue LEDs. The circuit of the RF power scavenger for (**A**) is on two stacked PCB boards that are connected with each other by a PCB connector. For RF power scavenger for (**B**), Au pre-patterned PI film supports all of components connected by silver epoxy.

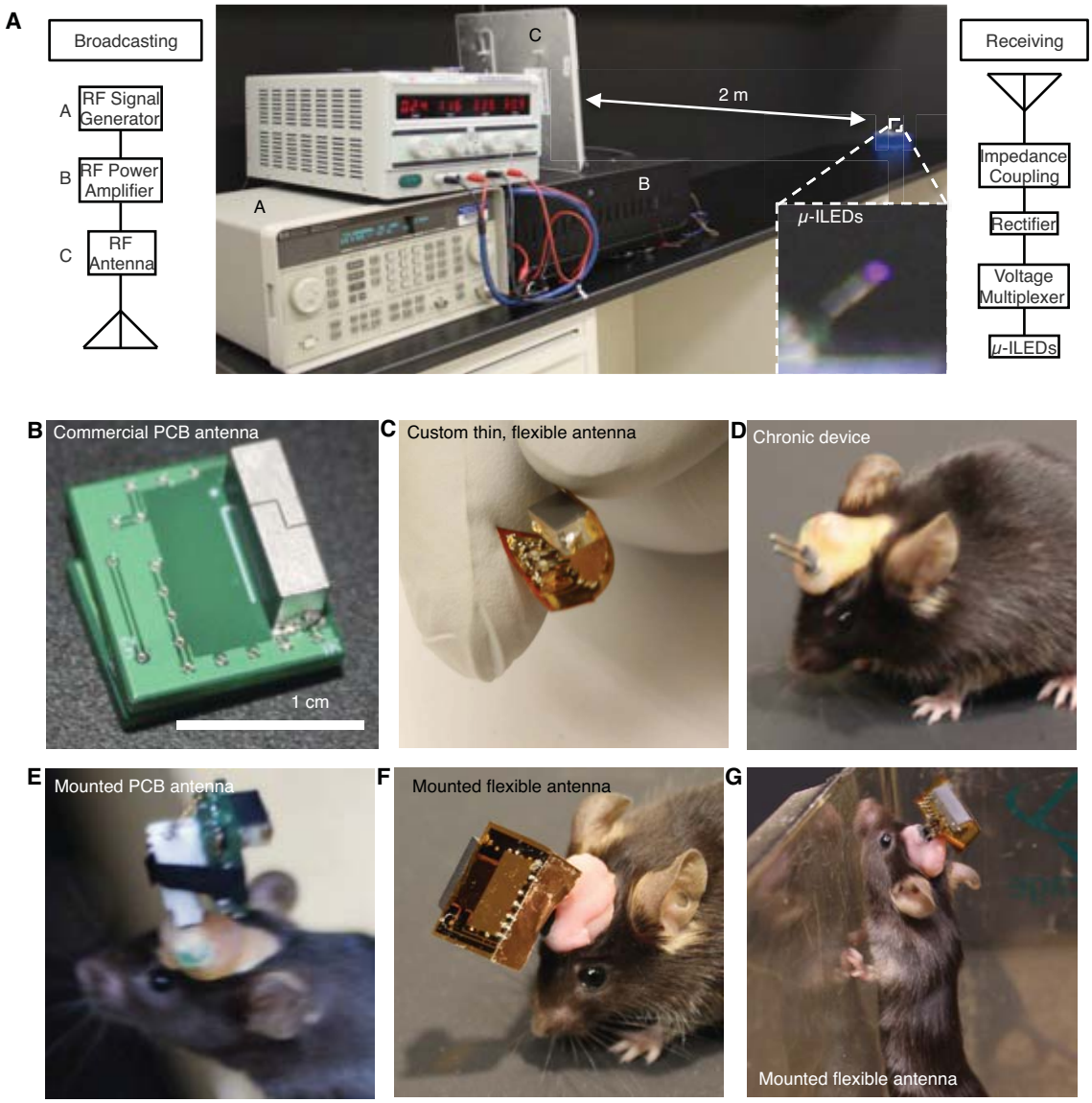

Figure S12

Key components for wireless operation using RF power delivery. **(A)** Photo and diagram explaining the components of the system and demonstrating wireless power. Headstage antennas on PCB board (**B**) and on bent PI (**C**). (**D**) A mouse with a chronically implanted device. The nature of the interconnect allows for temporary coupling to either form of headstage antenna or a wired power source. **(E,F,G)** Mice with acutely mounted headstage antennas.

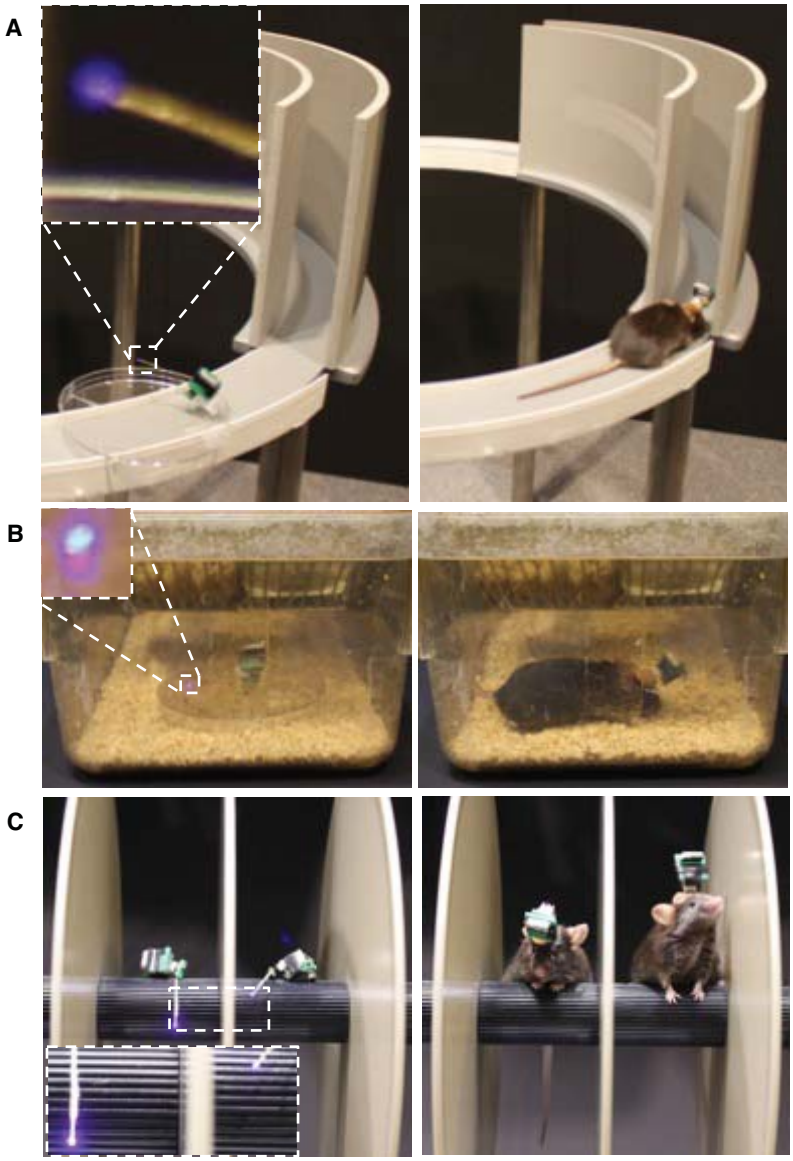

Figure S13
Demonstration of wireless capabilities. For all panels the same environment is shown with wireless lit μ-ILEDs (left) and wirelessly stimulated mice (right). (**A**) Wireless mice can explore circular environments with no need for commutators or adaptations to the behavioral apparatus. (**B**) RF modulation can be used to power devices through covered arenas as seen here with a mouse in a traditional homecage environment. (**C**) Multiple wireless devices can be controlled using a single antenna. Here, two implanted mice are receiving identical optical stimulation simultaneously on a standard rotarod- a rotating wheel that provides numerous barriers for use with tethered animals.

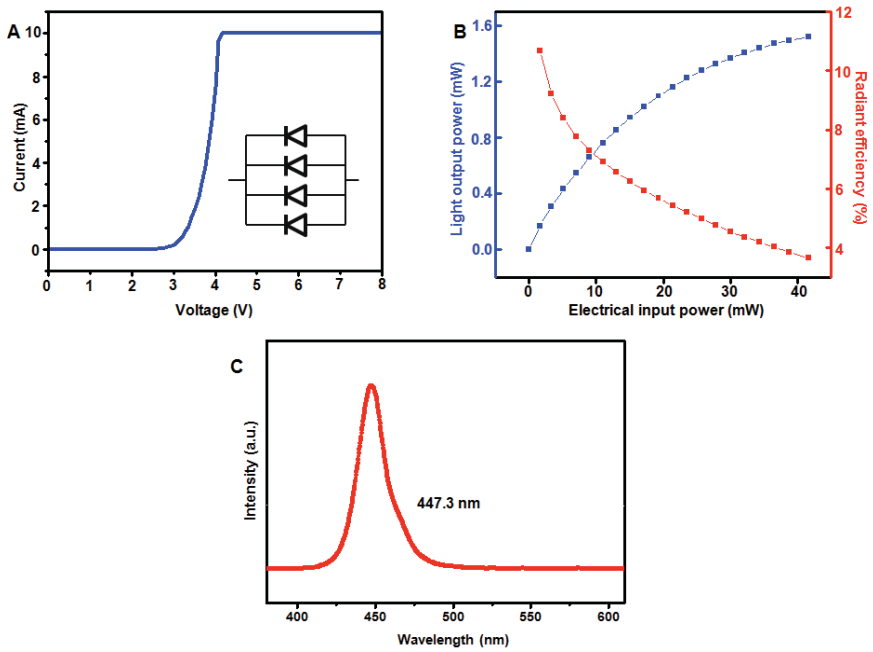

Figure S14

Electrical and optical properties of an array of four μ-ILEDs connected in parallel. **(A)** Current-Voltage (I-V) characteristics, **(B)** light output power and radiant efficiency as a function of electrical input power, and **(C)** light emission intensity as a function of wavelength.

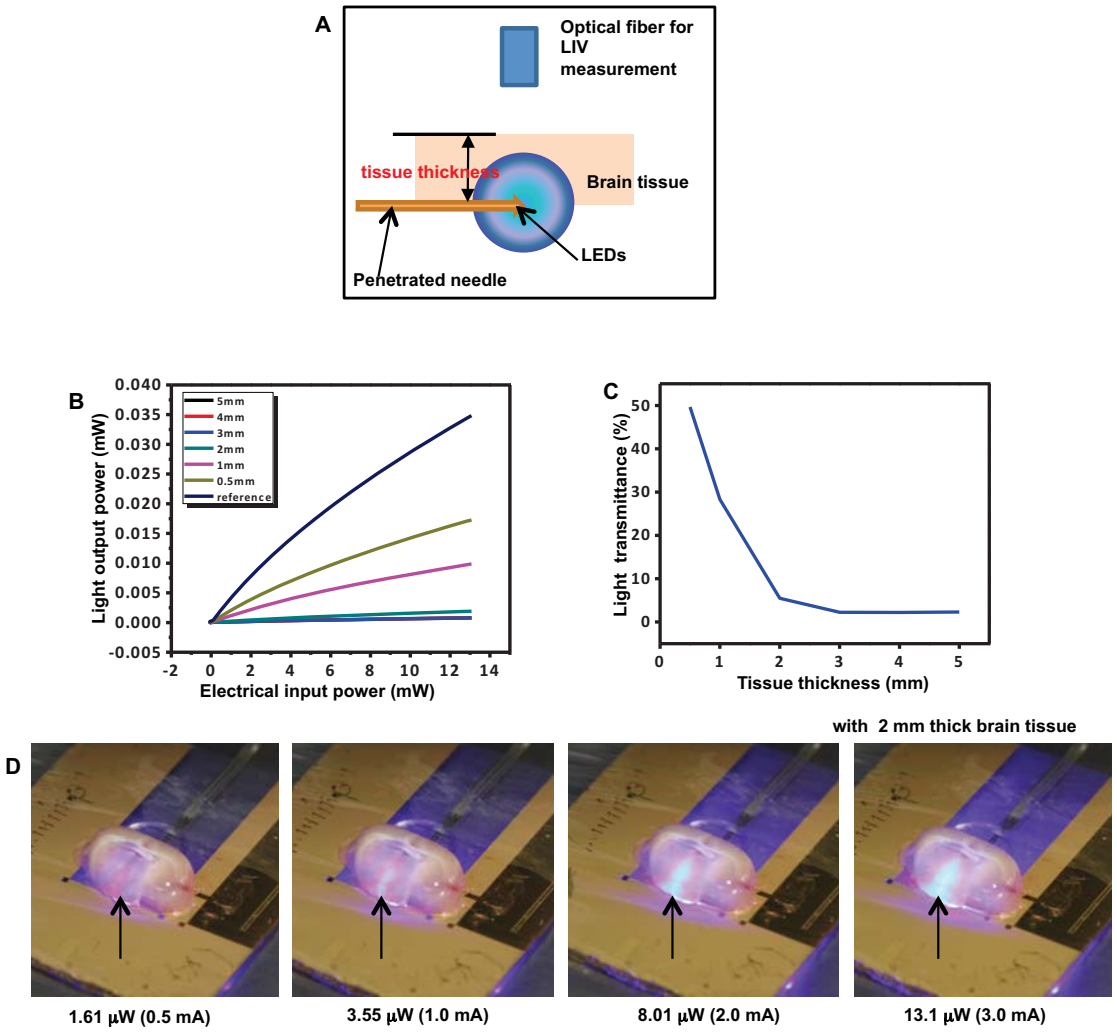

Figure S15

Information related to tests of light penetration depth. **(A)** Schematic illustration of the experimental scheme, **(B)** light output-current and voltage (LIV) results collected using slabs of brain tissue with various thicknesses (0.5, 1, 2, 3, 4, 5 mm) and **(C)** their light transmission through the thickness of the tissue. **(D)** Light extraction through 2 mm thick slabs of brain tissue at various applied powers.

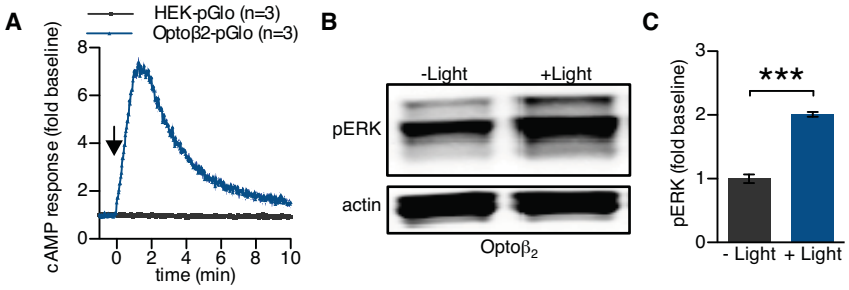

Figure S16

μ-ILED-induced activation of cAMP and ERK phosphorylation in Optoβ_2 expressing cells. **(A)** Optoβ_2 cells co-expressing pGlo show a rapid and transient increase in cAMP following light (450 nm, 5 sec, 0.5 W/cm^2 pulse) stimulation (n=3). HEK293 cells expressing pGlo show no response to the same light stimulation (n=3). Data are expressed as mean ± sem. **(B).** Representative pERK and actin Western Blots for Optoβ_2 and HEK293 cells following light (450 nm, 1 min, 0.5 W/cm^2 pulse) stimulation (n=3). **(C).** Quantitation of pERK normalized to actin in light stimulated Optoβ_2 and HEK293 cells. (*$p<0.05$, unpaired, two-tailed t-test).

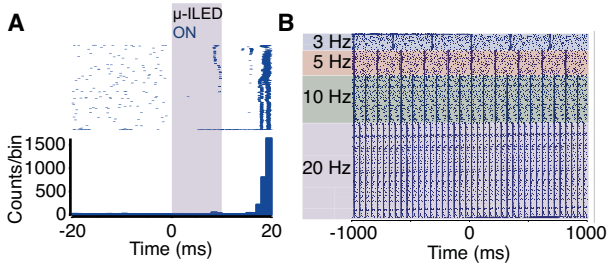

Figure S17
μ-ILED-induced modulation of *in vivo* neuronal activity in the VTA via ChR2(H134)-eYFP expressing neurons. **(A**) Representative peri-light raster plot and histogram demonstrating increased cell firing within 20 ms of onset of a 450 nm, 0.5 W/cm^2 light pulse. (**B**) Raster plot showing activity from the same neuron (A) time locking with various frequencies of light delivery. Each light pulse is centered at 0 ms, the effects of prior and subsequent pulses are apparent in each line of the 2000 ms raster plot.

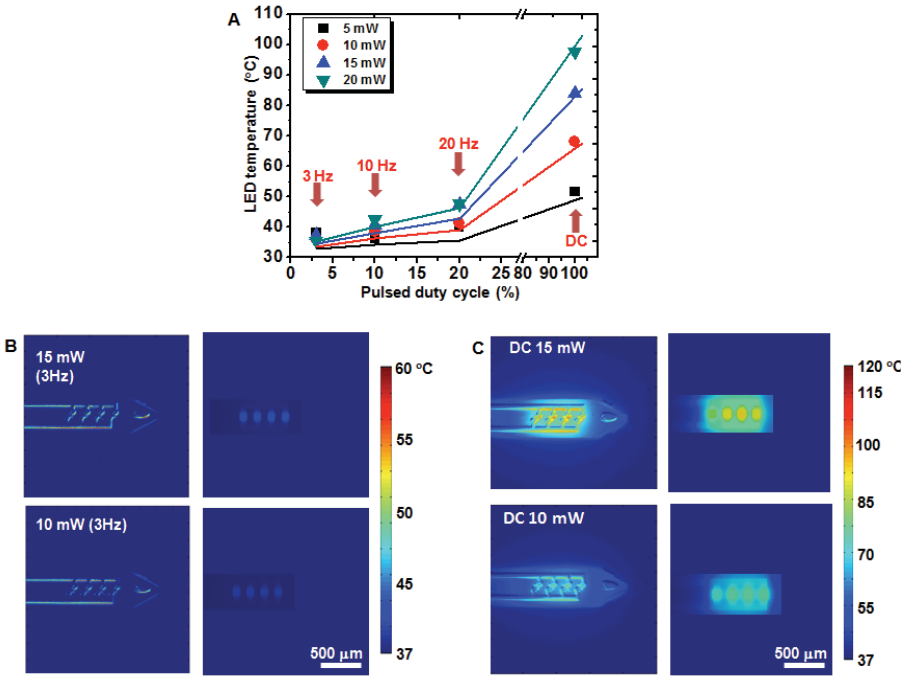

Figure S18

Surface temperature of μ-LEDs on an injection microneedle, during operation at various power levels in open air. **(A)** Measured (dots) and calculated (lines) temperatures of μ-ILEDs at various pulse duty cycles and at DC power levels. All calculated temperatures (lines) are obtained by time-average results at 37 ^{o}C background temperature. The duration time (width) for all pulsed cases is 10 msec. **(B)** Measured (left) and calculated (right) temperatures at 15 and 10 mW applied power. The measured (calculated) temperatures are 37.44 (39.31) and 36.15 (38.54) ^{o}C, respectively, with a 3 Hz pulse.
(C) Measured (left) and calculated (right) temperature at 15 and 10 mW DC applied power. The measured temperatures (calculated) are 84.01 (86.95) and 86.31 (70.30) ^{o}C, respectively, with a 3 Hz pulse.

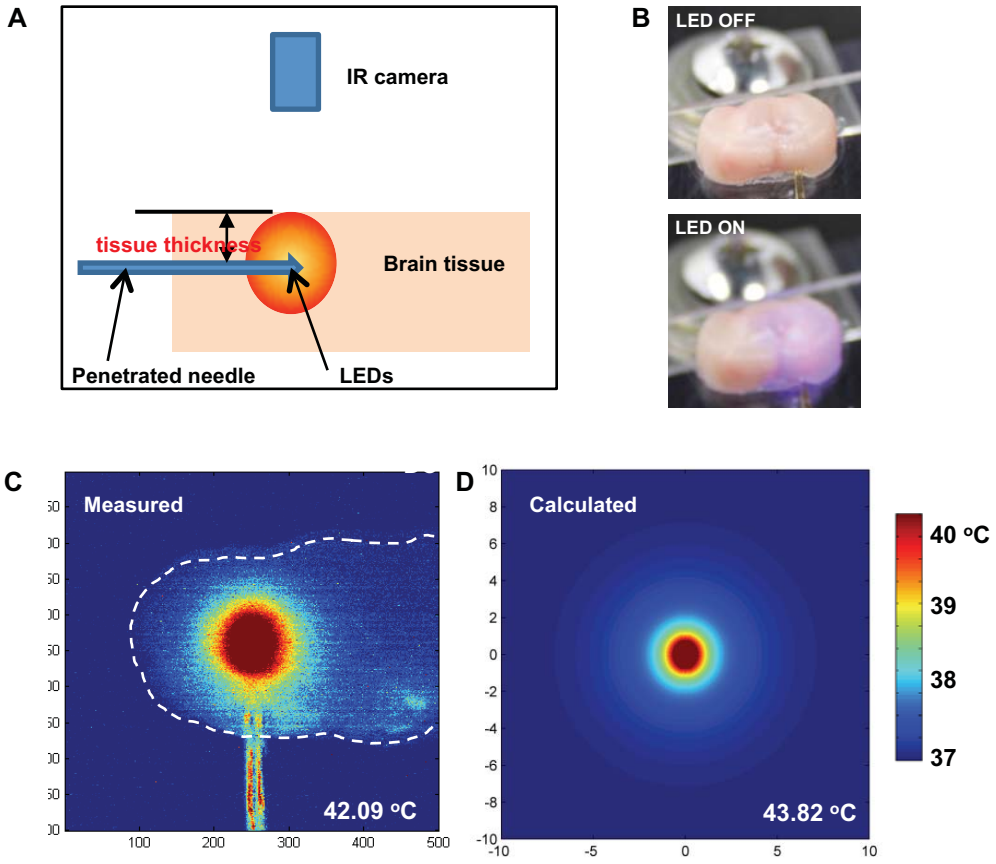

Figure S19

Thermal imaging with a calibrated IR camera. **(A)** Schematic illustration and **(B)** pictures of the IR camera stage and μ-ILED devices injected in brain tissue. **(C)** Measured and **(D)** calculated tissue temperature with μ-ILEDs injected into a 0.3 mm thick slab of tissue, evaluated at the surface for the case of 10 mW DC input power. Measured and calculated temperatures are 42.09 and 43.82 ^{o}C, respectively.

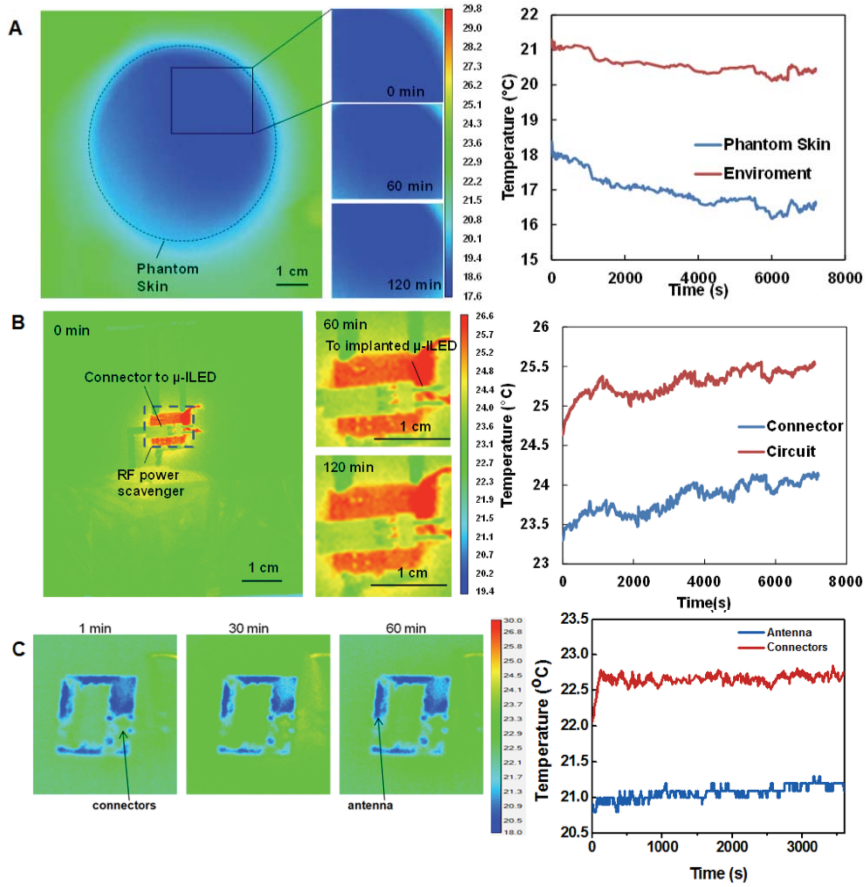

Figure S20

IR images (left) and extracted average temperatures (right) of a phantom skin sample and the surrounding environment during prolonged exposure to RF radiation, starting at time=0 s. The results indicate no observable effects of heating due to RF. The temperature variations in the phantom skin are small, and mostly due to variations in the environment, without any observable effect, even under constant RF power (**B**) IR images (left) of a RF power scavenger circuit during exposure to constant RF radiation for various times. The images show changes in temperature when RF power is applied, and the μ-ILEDs are turned on, for 0 (left), 60 (right, top), and 120 (right, bottom) min. Spatially averaged changes in temperature (right) of the RF power scavenger circuit and connector during prolonged exposure to constant RF radiation, starting at time=0 s. The temperature change is less than 0.5ºC during this 2 hr period. (**C**) IR images (left) of a thin, lightweight flexible RF power scavenger circuit during exposure to pulsed (10 Hz) RF radiation for various times: 1 (left), 30 (middle), and 60 (right) min. There is no temperature change (right) in the thin, lightweight flexible RF power scavengers (near the antenna and the connectors) during prolonged exposure to pulsed RF radiation at 10 Hz.

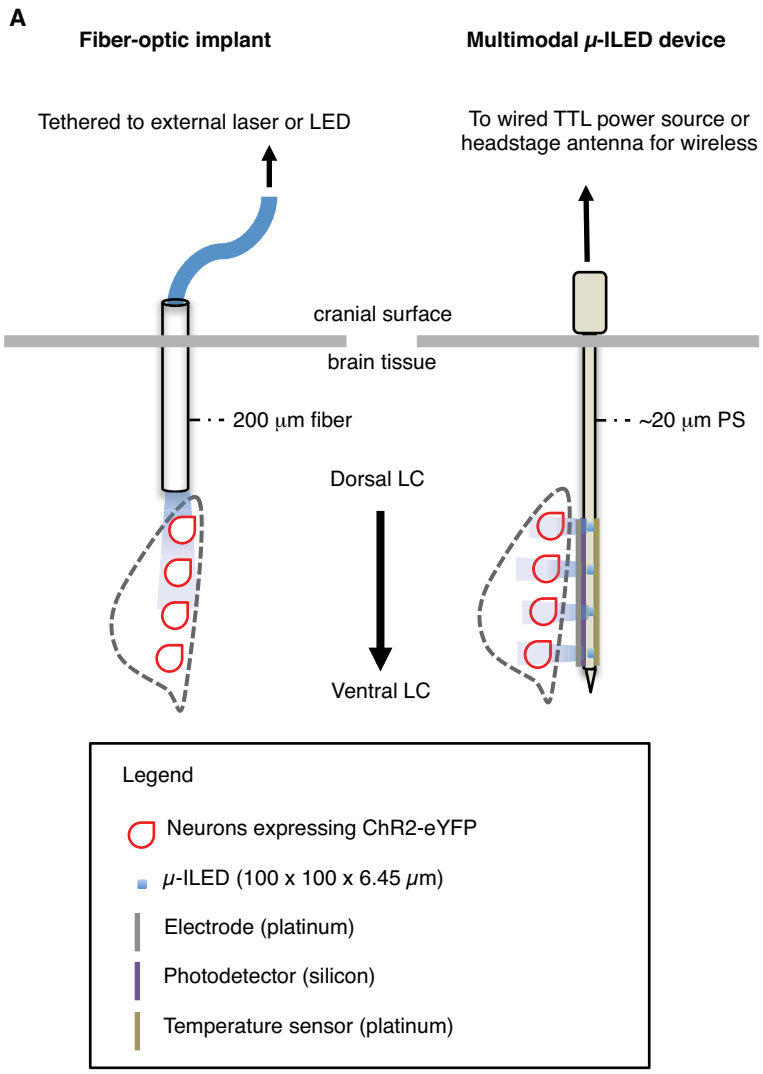

Figure S21

Cartoon depicting the experimental strategy used in Fig. 3B & 3C. μ-ILED devices allow for unique spatial targeting of brain structures (here the locus coeruleus) to provide consistent illumination along the entire dorsal-ventral plane of the structure.

Figure S22

The durability of the devices and the constituent component following chronic implantation. (**A**) Survival curve showing viability of μ-ILEDs, fully passivated sensors (temperature and μ-IPD), and animals following device injection. μ-ILEDs were considered viable if the all μ-ILEDs in each array were still emitting sufficient light to activated ChR2. Sensors were considered viable if performance was within 1% of original performance. Components performed reliably within the two-three week timespan of a normal behavioral experiment and often well beyond that range. Detailed information on each point of attrition or censorship is available in Table S1. **(B)** The μ-ILED devices are robust and capable of functioning properly months after implantation. Working devices one (top), three (center), and six (bottom) months after chronic implantation into freely moving mice.

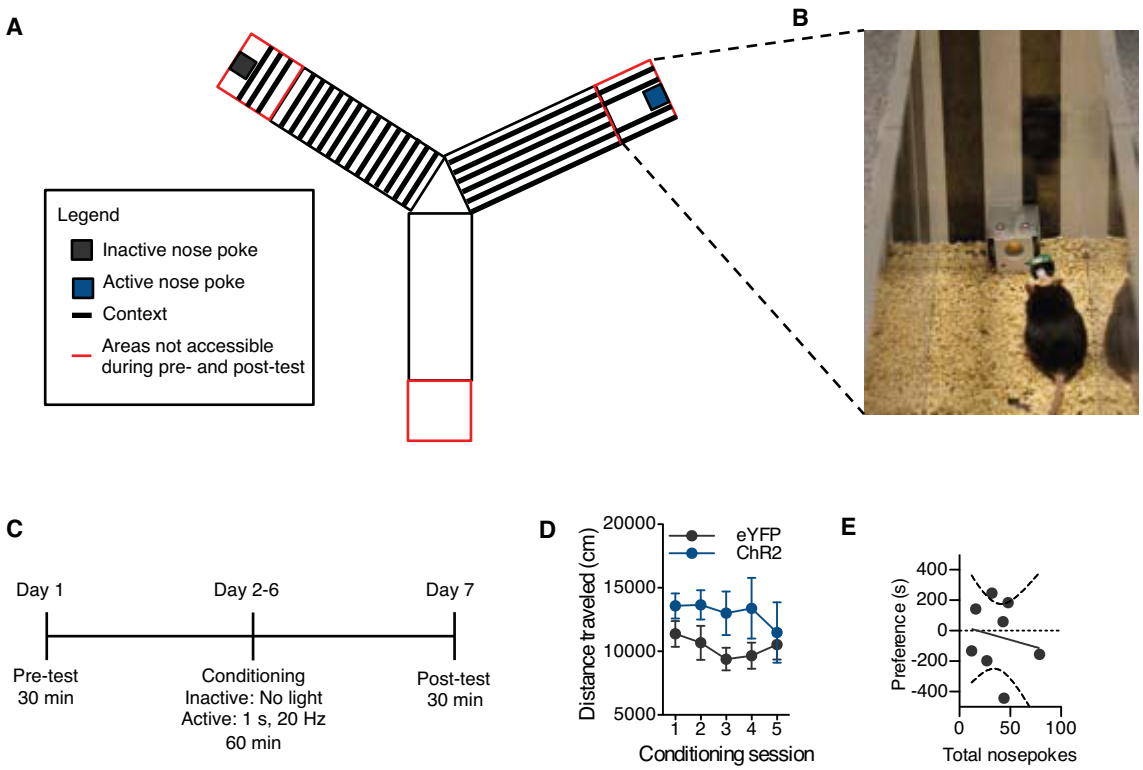

Figure S23
Wireless μ-ILED devices drive an operantly conditioned place preference. (**A**) Cartoon and (**B**) photo of Y-Maze with contexts and nose poke devices, red zones were not accessible during pre/post-tests. (**C**) Timeline of experimental approach. (**D**) Total activity during the conditioning shows increase in total ambulation of the ChR2 mice during the first four days of training. (**E**) Scatter plot demonstrating no correlation (r=-0.1707, p=0.6861) between post-test preference and total number of active nose pokes during training in the AAV-DIO-eYFP injected controls.

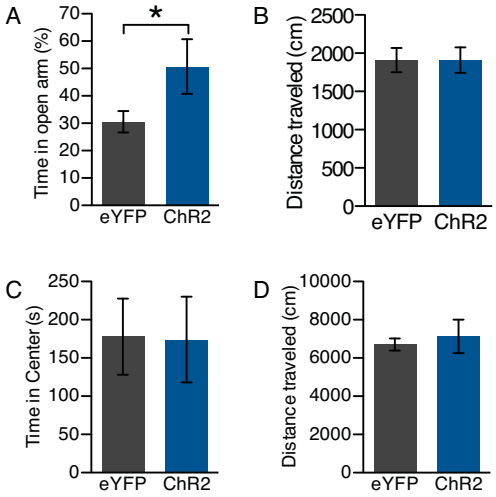

Figure S24

Tonic, not phasic, activation of VTA-DA neurons induces anxiolytic-like behavior. (**A**) 5 Hz activation of VTA-DA neurons induces an anxiolytic-like behavioral response in an elevated zero maze independent of (**B**) locomotor effects (n=6-9; *p<0.05 t test compared to AAV5-DIO-eYFP controls). (**C**) Phasic (20, 5 ms pulses of 20 Hz light every minute) stimulation does not influence anxiety-like behavior or (**D**) locomotor activity in the open field test (n=6-8/group).

Table S1
Detailed information on the attrition and censoring of devices from Figure S22A. The last working day after implantation was recorded as 0 if the damage occurred prior to or during implantation.

Device ID	Reason for attrition/censor	Last working day after implantation
S1	Testing period ended, sensor working	21
S2	Testing period ended, sensor working	21
S3	Testing period ended, sensor working	21
S4	Testing period ended, sensor working	21
S5	Testing period ended, sensor working	21
S6	Testing period ended, sensor working	220
S7	Interconnect failure	0
S8	Testing period ended, sensor working	7
L1	Structural damage during implantation	0
L2	Testing period ended, μ-ILEDs working	220
L3	Animal died, device damaged on removal	183
L4	Testing period ended, μ-ILEDs working	220
L5	Testing period ended, μ-ILEDs working	220
L6	Testing period ended, μ-ILEDs working	220
L7	Testing period ended, μ-ILEDs working	220
L8	Testing period ended, μ-ILEDs working	220
L9	Testing period ended, μ-ILEDs working	220
L10	Testing period ended, μ-ILEDs working	220
L11	Testing period ended, μ-ILEDs working	220
L12	Testing period ended, μ-ILEDs working	30
L13	Animal died, device damaged on removal	164
L14	One or more μ-ILED failure	186
L15	Testing period ended, μ-ILEDs working	90
L16	Testing period ended, μ-ILEDs working	90
L17	One or more μ-ILED failure	220
L18	One or more μ-ILED failure	220
L19	One or more μ-ILED failure	220
L20	One or more μ-ILED failure	220

Movie S1

A movie clip that illustrates the procedure for injecting ultrathin, mechanically compliant optoelectronics into the ventral striatum of an intact, living mouse brain. The movie specifically highlights the injection on the rigid microneedle and removal of the microneedle following dissolution of the silk adhesive. Total elapsed time between video clips is ~15 minutes.

References and Notes

1. D.-H. Kim *et al*., Dissolvable films of silk fibroin for ultrathin conformal bio-integrated electronics. *Nat. Mater.* **9**, 511 (2010). doi:10.1038/nmat2745 Medline

2. J. Viventi *et al*., A conformal, bio-interfaced class of silicon electronics for mapping cardiac electrophysiology. *Sci. Transl. Med.* **2**, 24ra22 (2010). doi:10.1126/scitranslmed.3000738 Medline

3. B. Tian *et al*., Three-dimensional, flexible nanoscale field-effect transistors as localized bioprobes. *Science* **329**, 830 (2010). doi:10.1126/science.1192033 Medline

4. D.-H. Kim *et al*., Epidermal electronics. *Science* **333**, 838 (2011). doi:10.1126/science.1206157 Medline

5. Q. Qing *et al*., Nanowire transistor arrays for mapping neural circuits in acute brain slices. *Proc. Natl. Acad. Sci. U.S.A.* **107**, 1882 (2010). doi:10.1073/pnas.0914737107 Medline

6. T. Sekitani, T. Someya, Stretchable organic integrated circuits for large-area electronic skin surface. *MRS Bull.* **37**, 236 (2012). doi:10.1557/mrs.2012.42

7. J. Ordonez, M. Schuettler, C. Boehler, T. Boretius, T. Stieglitz, Thin films and microelectrode arrays for neuroprosthetics. *MRS Bull.* **37**, 590 (2012). doi:10.1557/mrs.2012.117

8. S. C. B. Mannsfeld *et al*., Highly sensitive flexible pressure sensors with microstructured rubber dielectric layers. *Nat. Mater.* **9**, 859 (2010). doi:10.1038/nmat2834 Medline

9. T. Sekitani *et al*., Organic nonvolatile memory transistors for flexible sensor arrays. *Science* **326**, 1516 (2009). doi:10.1126/science.1179963 Medline

10. S. Takeuchi, T. Suzuki, K. Mabuchi, H. Fujita, 3D flexible multichannel neural probe array. *J. Micromech. Microeng.* **14**, 104 (2004). doi:10.1088/0960-1317/14/1/014

11. E. Stark, T. Koos, G. Buzsáki, Diode probes for spatiotemporal optical control of multiple neurons in freely moving animals. *J. Neurophysiol.* **108**, 349 (2012). doi:10.1152/jn.00153.2012 Medline

12. Y.-T. Kim, M. I. Romero-Ortega, Material considerations for peripheral nerve interfacing. *MRS Bull.* **37**, 573 (2012). doi:10.1557/mrs.2012.99

13. J. Mattis *et al*., Principles for applying optogenetic tools derived from direct comparative analysis of microbial opsins. *Nat. Methods* **18**, 159 (2011). doi:10.1038/nmeth.1808 Medline

14. P. Anikeeva *et al*., Optetrode: A multichannel readout for optogenetic control in freely moving mice. *Nat. Neurosci.* **15**, 163 (2011). doi:10.1038/nn.2992 Medline

15. H. Cao, L. Gu, S. K. Mohanty, J.-C. Chiao, An integrated μLED optrode for optogenetic stimulation and electrical recording. *IEEE Trans. Biomed. Eng.* **60**, 225 (2013). doi:10.1109/TBME.2012.2217395 Medline

16. B. Tian *et al*., Macroporous nanowire nanoelectronic scaffolds for synthetic tissues. *Nat. Mater.* **11**, 986 (2012). doi:10.1038/nmat3404 Medline

17. T.-I. Kim *et al*., High efficiency, microscale GaN light-emitting diodes and their thermal properties on unusually substrates. *Small* **8**, 1643 (2012). doi:10.1002/smll.201200382 Medline

18. Materials and methods are available as supporting material on *Science* Online.

19. Federal Communications Commission (FCC), *Guidelines for Evaluating the Environmental Effects of Radiofrequency Radiation* (FCC publication docket no. 93-62, 1996); http://transition.fcc.gov/Bureaus/Engineering_Technology/Orders/1996/fcc96326.txt.

20. R. D. Airan, K. R. Thompson, L. E. Fenno, H. Bernstein, K. Deisseroth, Temporally precise in vivo control of intracellular signalling. *Nature* **458**, 1025 (2009). doi:10.1038/nature07926 Medline

21. M. M. Elwassif, Q. Kong, M. Vazquez, M. Bikson, Bio-heat transfer model of deep brain stimulation-induced temperature changes. *J. Neural Eng.* **3**, 306 (2006). doi:10.1088/1741-2560/3/4/008 Medline

22. A. M. Aravanis *et al*., An optical neural interface: In vivo control of rodent motor cortex with integrated fiberoptic and optogenetic technology. *J. Neural Eng.* **4**, S143 (2007). doi:10.1088/1741-2560/4/3/S02 Medline

23. O. Yizhar, L. E. Fenno, T. J. Davidson, M. Mogri, K. Deisseroth, Optogenetics in neural systems. *Neuron* **71**, 9 (2011). doi:10.1016/j.neuron.2011.06.004 Medline

24. K. M. Tye *et al*., Amygdala circuitry mediating reversible and bidirectional control of anxiety. *Nature* **471**, 358 (2011). doi:10.1038/nature09820 Medline

25. A. N. Zorzos, J. Scholvin, E. S. Boyden, C. G. Fonstad, Three-dimensional multiwaveguide probe array for light delivery to distributed brain circuits. *Opt. Lett.* **37**, 4841 (2012). doi:10.1364/OL.37.004841 Medline

26. M. E. Carter *et al*., Tuning arousal with optogenetic modulation of locus coeruleus neurons. *Nat. Neurosci.* **13**, 1526 (2010). doi:10.1038/nn.2682 Medline

27. D. H. Szarowski *et al*., Brain responses to micro-machined silicon devices. *Brain Res.* **983**, 23 (2003). doi:10.1016/S0006-8993(03)03023-3 Medline

28. T. D. Y. Kozai, D. R. Kipke, Insertion shuttle with carboxyl terminated self-assembled monolayer coatings for implanting flexible polymer neural probes in the brain. *J. Neurosci. Methods* **184**, 199 (2009). doi:10.1016/j.jneumeth.2009.08.002

29. H. C. Tsai *et al*., Phasic firing in dopaminergic neurons is sufficient for behavioral conditioning. *Science* **324**, 1080 (2009). doi:10.1126/science.1168878 Medline

30. A. R. Adamantidis *et al*., Optogenetic interrogation of dopaminergic modulation of the multiple phases of reward-seeking behavior. *J. Neurosci.* **31**, 10829 (2011). doi:10.1523/JNEUROSCI.2246-11.2011 Medline

31. I. B. Witten *et al*., Recombinase-driver rat lines: Tools, techniques, and optogenetic application to dopamine-mediated reinforcement. *Neuron* **72**, 721 (2011). doi:10.1016/j.neuron.2011.10.028 Medline

32. K. M. Kim *et al*., Optogenetic mimicry of the transient activation of dopamine neurons by natural reward is sufficient for operant reinforcement. *PLoS ONE* **7**, e33612 (2012). doi:10.1371/journal.pone.0033612 Medline

33. T. M. McGranahan, N. E. Patzlaff, S. R. Grady, S. F. Heinemann, T. K. Booker, α4β2 nicotinic acetylcholine receptors on dopaminergic neurons mediate nicotine reward and anxiety relief. *J. Neurosci.* **31**, 10891 (2011). doi:10.1523/JNEUROSCI.0937-11.2011 Medline

34. L. Coque *et al*., Specific role of VTA dopamine neuronal firing rates and morphology in the reversal of anxiety-related, but not depression-related behavior in the *Clock*Δ19 mouse model of mania. *Neuropsychopharmacology* **36**, 1478 (2011). doi:10.1038/npp.2011.33 Medline

35. F. P. Incropera, D. P. Dewitt, T. L. Bergman, A. S. Lavine, *Fundamentals of Heat and Mass Transfer*, J. Hayton, Eds. (Wiley, New York, 2006).

36. B. Solano, S. Rolt, D. Wood, Thermal and mechanical analysis of an SU8 polymeric actuator using infrared thermography. *J. Mech. Eng. Sci.* **222**, 73 (2008). doi:10.1243/09544062JMES676

37. C. G. Mattsson *et al*., Development of an infrared thermopile detector with a thin selfsupporting SU-8 membrane, *IEEE SENSORS 2007 Conference*, 28 to 31 October *2007*, Atlanta, GA (2007), pp. 836–839.

38. A. K. van der Vegt, L. E. Govaert, *Polymeren, Van Keten Tot Kunststof* (Delft Univ. Press, Delft, Netherlands, 2005).

39. S. A. Campbell, *The Science and Engineering of Microelectronic Fabrication* (Oxford Univ. Press, New York, 2001).

40. A. Modafe, N. Ghalichechian, M. Powers, M. Khbeis, R. Ghodssi, Embedded benzocyclobutene in silicon: An integrated fabrication process for electrical and thermal isolation in MEMS. *Microelectron. Eng.* **82**, 154 (2005). doi:10.1016/j.mee.2005.07.005

41. B. Esler, T. Lyons, S. Turovets, D. Tucker, Instrumentation for low frequency EIT studies of the human head and its validation in phantom experiments. *J. Phys. Conf. Ser.* **224**, 012007 (2010). doi:10.1088/1742-6596/224/1/012007

42. K. Ito, K. Furuya, Y. Okano, L. Hamada, Development and characteristics of a biological tissue-equivalent phantom for microwaves. *Electron. Commun.* **84**, 67 (2001). doi:10.1002/1520-6424(200104)84:4<67::AID-ECJA8>3.0.CO;2-D

43. D. R. Sparta *et al*., Construction of implantable optical fibers for long-term optogenetic manipulation of neural circuits. *Nat. Protoc.* **7**, 12 (2011). doi:10.1038/nprot.2011.413 Medline

44. M. R. Bruchas *et al*., Selective p38α MAPK deletion in serotonergic neurons produces stress resilience in models of depression and addiction. *Neuron* **71**, 498 (2011). doi:10.1016/j.neuron.2011.06.011 Medline

45. N. R. Zhang *et al*., Serine 363 is required for nociceptin/orphanin FQ opioid receptor (NOPR) desensitization, internalization, and arrestin signaling. *J. Biol. Chem.* **287**, 42019 (2012). doi:10.1074/jbc.M112.405696 Medline

46. K. R. Tan *et al*., GABA neurons of the VTA drive conditioned place aversion. *Neuron* **73**, 1173 (2012). doi:10.1016/j.neuron.2012.02.015 Medline

47. A. M. Stamatakis, G. D. Stuber, Activation of lateral habenula inputs to the ventral midbrain promotes behavioral avoidance. *Nat. Neurosci.* **15**, 1105 (2012). doi:10.1038/nn.3145 Medline

48. S. Lammel *et al*., Input-specific control of reward and aversion in the ventral tegmental area. *Nature* **491**, 212 (2012). doi:10.1038/nature11527 Medline